Title: Thermal equation of state of post-aragonite $CaCO_3$-Pmmn
Manuscript Number: 7279R
Authors: Mingda Lv, Michigan State University Jiachao Liu, Michigan State University Eran Greenberg, Tel Aviv University Vitali Prakapenka, Consortium for Advanced Radiation Source (CARS) Susannah Dorfman, Michigan State University

Revision 1

Thermal equation of state of post-aragonite $CaCO_3$-*Pmmn*

Mingda Lv[1,*], Jiachao Liu[1], Eran Greenberg[2†], Vitali B. Prakapenka[2], Susannah M. Dorfman[1]

[1] Department of Earth and Environmental Sciences, Michigan State University, Michigan 48824, U.S.A.

[2] Center for Advanced Radiation Sources, The University of Chicago, Illinois 60439, U.S.A.

* Corresponding author

E-mail: lyumingd@msu.edu

† Present address: Applied Physics Department, Soreq Nuclear Research Center (NRC), Yavne 81800, Israel

Abstract

Calcium carbonate ($CaCO_3$) is one of the most abundant carbonates on Earth's surface and transports carbon to Earth's interior via subduction. Although some petrological observations support preservation of $CaCO_3$ in cold slabs to lower mantle depths, the geophysical properties and stability of $CaCO_3$ at these depths are not known, due in part to complicated polymorphic phase transitions and lack of constraints on thermodynamic properties. Here we measured thermal equation of state of $CaCO_3$-*Pmmn*, the stable polymorph of $CaCO_3$ through much of the lower mantle, using synchrotron X-ray diffraction in a laser-heated diamond-anvil cell up to 75 GPa and 2200 K. The room temperature compression data for $CaCO_3$-*Pmmn* are fit with third-order Birch-Murnaghan equation of state, yielding K_{T0} = 146.7 (±1.9) GPa and K_0' = 3.4(±0.1) with V_0 fixed to the value determined by *ab initio* calculation, 97.76 Å^3. High-temperature compression data are consistent with zero-pressure thermal expansion $\alpha_T = a_0 + a_1T$ with a_0 = 4.3(±0.3)×10^{-5} K^{-1}, a_1 = 0.8(±0.2)×10^{-8} K^{-2}, temperature derivative of the bulk modulus $(\partial K_T/\partial T)_P$ = -0.021(±0.001) GPa/K; the Grüneisen parameter γ_0 = 1.94(±0.02), and the volume independent constant q = 1.9(±0.3) at a fixed Debye temperature θ_0 = 631 K predicted via *ab initio* calculation. Using these newly determined thermodynamic parameters, the density and bulk sound velocity of $CaCO_3$-*Pmmn* and (Ca,Mg)-carbonate bearing eclogite are quantitatively modeled from 30 to 80 GPa along a cold slab geotherm. With the assumption that carbonates are homogeneously mixed into the slab, the results indicate the presence of carbonates in subducted slab is unlikely to be detected by seismic observations, and the source of buoyancy provided by carbonates is negligible to affect slab dynamics.

Keywords: carbonate, post-aragonite, thermal equation of state, lower mantle, X-ray diffraction

Introduction

Calcium carbonate ($CaCO_3$) in the form of calcite is one of the most abundant carbonates on Earth's surface (reviewed by Luth, 1999), and an important vector of carbon to Earth's interior. Calcite can be sequestered in the oceanic crust by hydrothermal alteration and biological activity, and transferred to the mantle in subducting slabs (Dasgupta and Hirschmann, 2010; Kelemen and Manning, 2015; Staudigel, 2014). However, four major chemical processes have been argued to block transport of $CaCO_3$ transport to the lower mantle: 1) melting of carbonate and carbonated peridotite or eclogite (e.g., Dasgupta and Hirschmann, 2006; Ghosh et al., 2014; Kiseeva et al., 2013; Thomson et al., 2016), 2) reduction of carbonate solid or melt through reaction with iron or other reduced phases, generating diamond (e.g., Dorfman et al., 2018; Palyanov et al., 2013; Rohrbach and Schmidt, 2011), 3) carbonate-silicate exchange consuming $CaCO_3$ to form Ca-perovskite and $MgCO_3$ (e.g., Biellmann et al., 1993; Seto et al., 2008), 4) decarbonation of $CaCO_3$ with free silica phase to form Ca-perovskite, CO_2 or C (e.g., Drewitt et al., 2019; Li et al., 2018). Whether the energetics and kinetics of these reactions lead to complete loss of $CaCO_3$ from very cold and/or fast subducting slabs has been controversial (e.g., Martirosyan et al., 2016; Zhu et al., 2019), though superdeep diamonds with $CaCO_3$ inclusions coexisting with lower mantle phases such as $CaSiO_3$ perovskite (Brenker et al., 2007; Bulanova et al., 2010; Tschauner et al., 2018) prove the existence of $CaCO_3$ in at least some regions of the transition zone and lower mantle. To determine the conditions needed to preserve $CaCO_3$ in these regions and its fate during subduction to the mantle, experimental constraints on thermodynamic behavior of $CaCO_3$ are needed at lower-mantle conditions.

At mantle pressure and temperature (*P*-*T*) conditions, multiple polymorphic phase transitions of $CaCO_3$ have recently been discovered and debated, with potentially important

effects on melting and other chemical reactions in the mantle. Calcite is stable up to ~3 GPa and then transforms to aragonite with space group *Pnma* ($CaCO_3$-*Pnma*), which remains stable through the transition zone and shallow lower mantle (e.g., Litasov et al., 2017). The reported melting curve of $CaCO_3$-*Pnma* and a mixture of $CaCO_3$-$MgCO_3$ are higher than a hot slab geotherm (Li et al., 2017; Thomson et al., 2014), suggesting that subducted $CaCO_3$ may survive melting in the transition zone and travel to the lower mantle. At lower mantle pressures, the post-aragonite structures have been a subject of active recent research, and experimental studies from ~40 to 50 GPa have identified 1 transition to an orthorhombic structure, or transitions to an intermediate monoclinic structure then an orthorhombic structure. The orthorhombic structure is most commonly termed "post-aragonite" ($CaCO_3$-*Pmmn*), which was first identified by (Ono et al., 2005) at ~40 GPa and confirmed by computational structure simulations (Oganov et al., 2006). More recently, a monoclinic $P2_1/c$ structure ($CaCO_3$-$P2_1/c$-1, "-l" = low-pressure) was predicted to be an intermediate stable phase from ~40 to 50 GPa between $CaCO_3$-*Pnma* and $CaCO_3$-*Pmmn* (Gavryushkin et al., 2017; Pickard and Needs, 2015; Smith et al., 2018). $CaCO_3$-$P2_1/c$-1 was observed experimentally by (Gavryushkin et al., 2017; Li et al., 2018; Smith et al., 2018), but the transition from monoclinic to $CaCO_3$-*Pmmn* was found to be kinetically challenging (Smith et al., 2018). Near the base of Earth's mantle, $CaCO_3$ is expected to transform from one of these sp^2-hybridized post-aragonite structures to one of multiple proposed sp^3-hybridized post-post-aragonite structures. The first sp^3-hybridized post-post-aragonite to be identified was a pyroxene-structured $C222_1$ phase ($CaCO_3$-$C222_1$) observed at pressures higher than 130 GPa, corresponding to conditions near the core-mantle boundary (Oganov et al., 2006; Oganov et al., 2008; Ono et al., 2007). A second monoclinic $P2_1/c$ structure with sp^3-hybridization, termed $CaCO_3$-$P2_1/c$-h ("-h" = high-pressure, to distinguish it from the lower-

pressure "-1" polymorph), was predicted to be more favorable than $CaCO_3$-$C222_1$ (Pickard and Needs, 2015) and observed at pressures as low as ~105 GPa (Lobanov et al., 2017). Although the stable forms of $CaCO_3$ at the top and bottom of the lower mantle and conditions of the sp^2- to sp^3-hybridization transition in $CaCO_3$ remain controversial, $CaCO_3$-*Pmmn* is thought to be the stable phase of $CaCO_3$ throughout most of the lower mantle (see phase diagram of $CaCO_3$ proposed by Gavryushkin et al., 2017; Smith et al., 2018; Zhang et al., 2018).

The stability and abundance of $CaCO_3$-*Pmmn* can be modeled in the Earth using constraints on thermoelastic behavior, including accurate thermal equation of state (TEoS) measurements and corresponding thermoelastic parameters bulk modulus, its pressure and temperature derivatives, and thermal expansion coefficient. However, in contrast to the relatively well-known thermoelastic behavior of $CaCO_3$-*Pnma* (Li et al., 2015; Litasov et al., 2017; Palaich et al., 2016; Ye et al., 2012), experimental and computational constraints on the equation of state (EoS) of $CaCO_3$-*Pmmn* have been limited to 300 K (Lobanov et al., 2017; Ono et al., 2005) and 0 K (Oganov et al., 2006), respectively, without addressing high-temperature expansion behavior. In order to accurately model the phase equilibrium and physical properties of $CaCO_3$ at lower mantle conditions, the TEoS study on $CaCO_3$-*Pmmn* is required.

In this study, we investigate the structural stability of $CaCO_3$-*Pmmn*, and establish its TEoS up to 75 GPa and 2200 K using synchrotron X-ray diffraction in a laser-heated diamond anvil cell (LHDAC). The physical properties of $CaCO_3$ along cold subducting slab geotherm are calculated using the TEoS parameters, which are compared with the other major endmember carbonate, $MgCO_3$. By combining the newly obtained parameters with literature thermodynamic parameters of mineral phases in the subducted slab, we model the effect of the presence of

$CaCO_3$-$MgCO_3$ mixture on the density and bulk sound velocity of the carbonate-rich subducting slab at lower mantle conditions.

Experimental methods

$CaCO_3$-*Pmmn* was synthesized from calcite under high pressure and temperature conditions using a LHDAC. Sample material was prepared by mixing calcite powder (99.95%, Alfa Aesar) with 5 wt% micron-scale Au powder (99.95%, Goodfellow), which serves as a laser absorber and pressure calibrant. The mixture was mechanically ground under ethanol for 1 hour, then dried in an oven at 120 °C overnight to remove moisture contamination. The powder was slightly compressed to form a ~10-μm-thick disc for loading into the DAC. We use a symmetric DAC equipped with a pair of 150-μm culet beveled anvils to generate high pressures. A rhenium gasket of 250 μm thick was pre-indented to ~25-μm, and a hole with 75-μm diameter was drilled in the center of the indentation, serving as the sample chamber. To separate the sample disc from the diamond anvils, we loaded a sample disc into the sample chamber supported by three small ~5 μm-thick calcite spacers. To achieve quasi-hydrostatic conditions in the sample chamber, Ne was loaded as pressure transmitting medium and thermal insulator using the COMPRES/GSECARS gas-loading system (Rivers et al., 2008).

The TEoS of $CaCO_3$-*Pmmn* was determined using synchrotron X-ray diffraction with in-situ laser heating carried out at beamline 13-ID-D of the GeoSoilEnviroCARS sector of the Advanced Photon Source (APS), Argonne National Laboratory (ANL). The monochromatic X-ray beam with a wavelength of 0.3344 Å was focused on an area of ~2.5 × 3 μm^2 on the sample. Each two-dimensional X-ray diffraction image was recorded on a CdTe 1M Pilatus detector for 30 s, and subsequently integrated using Dioptas software (Prescher and Prakapenka, 2015). The sample-to-detector distance, tilt, and rotation of the detector relative to the incident X-ray beam

were calibrated using the diffraction pattern of LaB_6 powder at ambient conditions. The sample was heated using a double-sided Nd:YLF laser heating system (Prakapenka et al., 2008). Two 1.064 μm laser beams were focused to 20-μm diameter on both sides of the sample, and co-axially aligned with the incoming X-ray beam by using the X-ray-induced luminescence on the sample. Temperatures during heating were determined by fitting the measured thermal radiation spectra using the Planck radiation function under the graybody approximation (Prakapenka et al., 2008). The uncertainty of temperatures is ±100 K up to 2000 K and ±150 K higher than 2000 K based on multiple temperature measurements from both sides of the laser-heated sample. Pressures were calculated using the TEoS of the Au standard (Fei et al., 2007), with uncertainties propagating from that of temperatures, unit-cell volumes of Au, and TEoS parameters of Au, and the unit-cell volumes of Au were derived from diffraction lines (1 1 1), (2 0 0), (2 2 0) and (3 1 1) (Fig. 1 and 2).

Results and discussion

Synthesis and stability of $CaCO_3$-*Pmmn*

The starting material calcite was directly compressed in a DAC to the target pressure of 49 GPa before laser heating to synthesize the stable lower-mantle form of $CaCO_3$. During heating at 1800 K and after quench to 300 K, $CaCO_3$-*Pmmn* was confirmed by full-profile refinement XRD using the Le Bail method (Le Bail et al., 1988) as implemented in the GSAS/EXPGUI program (Toby, 2001) (Fig. 1). In contrast, some previous studies which attempted synthesis from $CaCO_3$-*Pnma* or $CaCO_3$-$P2_1$/c-l (Gavryushkin et al., 2017; Smith et al., 2018) failed to obtain complete transformation to $CaCO_3$-*Pmmn*, perhaps due to thermal gradients during laser heating and/or high kinetic barriers to transitions between these structures.

Sharp diffraction peaks of Au after annealing and intense diffraction from Ne pressure medium support quasi-hydrostatic stress conditions in the sample chamber (Fig. 1 and 2). An additional diffraction peak is observed at *d*-spacing of 2.6 Å, which broadens with increasing pressure and disappears above 60 GPa, probably representing metastable $CaCO_3$-$P2_1/c$-l retained due to phase transition kinetics (Bayarjargal et al., 2018; Gavryushkin et al., 2017; Li et al., 2018; Smith et al., 2018). The unit-cell parameters of $CaCO_3$-*Pmmn* at 300 K and 49 GPa are consistent with previous observations (Gavryushkin et al., 2017; Ono et al., 2005) within the uncertainty of pressure calibration (Fig. 1). As pressure and temperature increased, in-situ XRD exhibits no splitting or broadening of $CaCO_3$-*Pmmn* peaks, indicating no melting, dissociation or phase transition occurred (Fig. 1 and 2). This study concurs with other previous studies (e.g., Gavryushkin et al., 2017; Oganov et al., 2006; Ono et al., 2005) that $CaCO_3$-*Pmmn* is the stable form of $CaCO_3$ up to 75 GPa and 2200 K.

After synthesis of $CaCO_3$-*Pmmn*, we further compressed the sample at ~2-3 GPa intervals from 50 to 75 GPa, the minimum range of stability of this phase (Gavryushkin et al., 2017; Smith et al., 2018; Zhang et al., 2018). At each target pressure, we collected XRD patterns of the sample at 300 K before and after heating, and collected high-temperature patterns while the temperature was increasing at ~50-100 K intervals from ~1000 to 2200 K (Fig. 2). The lattice parameters of $CaCO_3$-*Pmmn* were obtained by least-squares fitting of diffraction lines (1 1 1), (0 2 0), (2 0 0) and (0 2 1) by using PDIndexer software (Seto et al., 2010), and are provided in the Table S1.

To directly compare volumes observed at 300 K for $CaCO_3$-*Pmmn* to previous studies (Lobanov et al., 2017; Ono et al., 2005), we recalculated previously-reported pressures using the Pt scale of Fei et al. (2007) for consistency with Au scale applied in this study (Fig. 3a). With

this correction, all *P*-*V* data are consistent within uncertainty over the pressure range examined in this work.

Compressibility of $CaCO_3$-*Pmmn* at 300 K

Because all previous compression data for $CaCO_3$-*Pmmn* were obtained at room temperature only, and the room temperature isotherm provides a useful constraint on the *P*-*V*-*T* EoS, we first address the 300 K *P*-*V* EoS of $CaCO_3$-*Pmmn*. *P*-*V* data of $CaCO_3$-*Pmmn* obtained at 300 K were fit to a third-order Birch-Murnaghan equation of state (BM3 EoS) (Birch, 1952) using the error-weighted least squares method to constrain zero-pressure parameters unit-cell volume (V_0), bulk modulus (K_{T0}) and its pressure derivative (K_0') (Fig. 3a and Table 1). We first fit the data using BM3 EoS without constraints on parameters, yielding V_0 = 96.6(±4.8) Å^3, K_{T0} = 162(±62) GPa, K_0' = 3.1(±1.1). The large uncertainties in fitted parameters reflect the long extrapolation from high-pressure data to 1 bar for this unquenchable phase, but compressibility at mantle-relevant pressures is well-constrained.

Previous experimental studies (Ono et al., 2005, Lobanov et al., 2017) reported EoS parameters that may differ due to different scales used to determine pressure, extrapolation to 1 bar, and the choice to fix $K_0' = 4$, as well as differences in hydrostatic conditions due to choice of pressure media. Experimental volumes obtained by Lobanov et al. (2017) without a pressure medium above ~90 GPa are high relative to our extrapolated EoS even with pressures corrected to match the pressure scale in this study (Fig 3a), corresponding to a relatively high incompressibility at mantle pressures. However, the incompressibility K_{T0} reported by both previous studies is relatively low compared to our unconstrained fit. This parameter trades off with relatively high V_0 and K_0' in these studies. Since $CaCO_3$-*Pmmn* is an unquenchable phase

and reverts to calcite upon decompression (Ono et al., 2005), the unit-cell volume at ambient pressure cannot be measured directly, which leads to large uncertainties on the 1 bar parameters. We therefore also fit our 300 K data setting 50 GPa as the reference pressure and obtain K_{50} = 302(±15) GPa, K'_{50} = 2.1(±1.7) and V_{50} = 77.526(±0.046) Å^3. A fit to the 300 K data from Ono et al. (2005) and Lobanov et al. (2017) setting 50 GPa as the reference pressure yields larger K_{50} (Fig 3b). This difference is consistent with less hydrostatic conditions in the sample chamber provided by NaCl medium in Ono et al. (2005) and no pressure medium in Lobanov et al. (2017) relative to the quasi-hydrostatic conditions provided by Ne medium and frequent annealing in this study.

Analysis of the finite Eulerian strain corresponding to compression behavior of $CaCO_3$-*Pmmn* supports the low K'_0 from the BM3 EoS. *P*-*V* data can be described by the normalized stress ($f_E = [(V_0/V)^{2/3}-1]/2$) versus the finite Eulerian strain ($F_E = P/[3f_E(1+2f_E)^{5/2}]$) plot (Fig. 4), where $F_E = K_{T0} + 1.5\ K_{T0}f_E(K'_0 - 4)$. The intercept value, $F_E(0)$ = 162(±2) GPa, agrees with K_{T0} obtained from the fit to the BM3 EoS, and the negative slope indicates K'_0 is smaller than 4 (Angel, 2000), which is consistent with our fitting results.

The EoS obtained by DFT-GGA (Oganov et al., 2006) and DFT-LDA (Marcondes et al., 2016) serve as upper and lower bounds of experimental measurements, respectively (Fig. 3a). (Marcondes et al., 2016) provide the only previous predictions of the elastic shear properties of $CaCO_3$-*Pmmn*, which are necessary to directly compare our results for thermoelastic parameters derived by MGD EoS (discussed in the following section). We thus provide an additional fit to our 300 K *P*-*V* data with V_0 fixed to 97.76 Å^3 as predicted by DFT-LDA, yielding K_{T0} = 146.7 (±1.9) GPa and K'_0 = 3.4(±0.1). Smaller K_{T0} and larger K'_0 relative to the unconstrained BM3 EoS

are mainly due to the tradeoffs between V_0, K_{T0}, and K_0' (Fig. S1). The modeled K_T at pressures from 50-80 GPa (black dashed line in Fig. 3b) are consistent with the fits without a fixed V_0.

Thermal equation of state of $CaCO_3$-*Pmmn*

To constrain the TEoS, unit-cell volumes for $CaCO_3$-*Pmmn* are collected up to 75 GPa and 2200 K (Table. S1), with temperature determined by spectroradiometry and pressure measured using the TEoS of Au (Fei et al., 2007). We use two approaches to constrain high-temperature behavior: 1) obtaining thermal expansion coefficient (α_T) from fitting *P-V-T* data to a high-temperature BM3 EoS (HT-BM3 EoS) (Birch, 1952; Fei, 1995) (Fig. 5a), and 2) obtaining Grüneisen parameter (γ_0) from a Mie-Grüneisen-Debye equation of state (MGD EoS) (Jackson, 1998; Jackson and Rigden, 1996) (Fig. 5b). Both the MGD EoS and HT-BM3 EoS models can mathematically describe our experimental measurements well (Fig. 5), but have complementary strengths and weaknesses in terms of fitting tradeoffs, assumptions, and sensitivity to physically meaningful quantities. To be more specific, the MGD EoS formulation is based on statistical mechanics, i.e., Debye's approximation, but is not directly comparable to experiments; whereas the HT-BM3 EoS formulation is based on finite strain theory to empirically express experimental measurements, but can lead to poor extrapolation beyond experimental conditions (Poirier, 2000). Both models have been widely applied to materials in Earth sciences with thermodynamic databases used in geophysical studies, such as (Fabrichnaya et al., 2004) based on HT-BM3 EoS, and (Stixrude and Lithgow-Bertelloni, 2011) based on MGD EoS. We present both models to allow the reader to assess the effects of tradeoffs, and to directly use and compare our results to the previous results in these thermodynamic databases.

The HT-BM3 EoS is given by the following expression for $P(V, T)$:

$$P(V,T) = \left(\frac{3}{2}\right) K_T \left[\left(\frac{V_{T,0}}{V}\right)^{\frac{7}{3}} - \left(\frac{V_{T,0}}{V}\right)^{\frac{5}{3}}\right]\left\{1 + \frac{3}{4}(K_T' - 4)\left[\left(\frac{V_{T,0}}{V}\right)^{\frac{2}{3}} - 1\right]\right\},$$

where K_T denotes isothermal bulk modulus at ambient pressure and a given high temperature, $V_{T,0}$ is the ambient pressure volume, V is the high-pressure and temperature volume, and K_T' is the pressure derivative of K_{T0} at ambient pressure, neglecting higher-order pressure derivatives of the bulk modulus and assuming that K_T' is a constant in the temperature range of our study, i.e., K_0'. The temperature effect on K_T can be expressed as a linear function of temperature, with the temperature derivative at ambient pressure $(\partial K_T/\partial T)_P$ and K_{T0} as follow:

$$K_T = K_{T0} + (\partial K_T/\partial T)_P (T - T_0),$$

where T_0 is the reference temperature, 300 K. $(\partial K_T/\partial T)_P$ is assumed to be a constant within the temperature range of our study. The temperature dependence of the volume at ambient pressure, $V_{T,0}$, can be expressed as a function of the thermal expansion at zero pressure:

$$V_{T,0} = V_0 \exp\left(\int_{T_0}^{T} \alpha_T dT\right).$$

The thermal expansion coefficient α_T is expressed as $\alpha_T = (1/V)(\partial V/\partial T)_P$. At atmospheric pressure, α_T can be approximated to a linear function of temperature:

$$\alpha_T = a_0 + a_1 T,$$

where a_0 and a_1 are constants. By least-squares fitting with the parameters V_0, K_{T0} and K_0' fixed from the 300 K BM3 EoS, we obtained a_0, a_1, and $(\partial K_T/\partial T)_P$. We further fit the P-V-T data with a fixed V_0 to 97.76 Å^3 alone, yielding K_{T0}, K_0', a_0, a_1, and $(\partial K_T/\partial T)_P$, which are consistent with the first fitting within uncertainties (Table 2). The isothermal compression curves for temperatures from 1300 to 2200 K at 300 K intervals were calculated from these thermoelastic parameters (Fig. 5a). The fitting residuals indicate the discrepancies between measured and calculated pressure are ranging from -1.7 to 1.4 GPa within the investigated pressure and

temperature range (Fig. 5a), indicating the fitted HT-BM3 EoS can describe our experimental measurements well.

In the MGD EoS, the total pressure $P(V,T)$ is expressed as the sum of the static pressure at room temperature, $P(V,T_0)$, and the thermal pressure, $P_{th}(V,T)$:

$$P(V,T) = P(V,T_0) + P_{th}(V,T),$$

where $P(V,T_0)$ is fixed by BM3 EoS at 300 K, and the thermal pressure $P_{th}(V,T)$ is a function of the Grüneisen parameter γ and the thermal energy $E_{th}(V,T)$, that can be estimated using a Debye model:

$$P_{th}(V,T) = \frac{\gamma(V,T)}{V}[E_{th}(V,T) - E_{th}(V,T_0)],$$

$$E_{th}(V,T) = \frac{9\mathrm{nR}T}{(\theta/T)^3}\int_0^{\theta/T}\frac{x^3}{e^x-1}dx,$$

where θ is the Debye temperature, n = 5 is the number of atoms in the formula unit, and R is the gas constant (8.314 J·mol^{-1}·K^{-1}). The volume dependence of the θ and γ are described by:

$$\theta = \theta_0\, exp\left(\frac{\gamma_0-\gamma}{q}\right),$$

$$\gamma = \gamma_0\left(\frac{V}{V_0}\right)^q,$$

where q is the dimensionless power mode parameter, γ_0 and θ_0 are Grüneisen parameter and Debye temperature at 300 K, respectively. As above, V_0, K_{T0}, K_0' are fixed from the 300 K EoS. The θ_0 can be evaluated more precisely from sound velocities using equations based on Debye's lattice vibration model (Poirier, 2000). With self-consistent elastic parameters at zero pressure K_{S0} = 122 GPa, G_0 = 56 GPa and ρ_0 = 3.4 g/cm^3 reported by (Marcondes et al., 2016), the θ_0 for $CaCO_3$-*Pmmn* was estimated to be 631 K. Due to strong correlations between the three high-temperature parameters θ_0, γ_0 and q, we fixed θ_0 and obtained the fitted γ_0 = 1.94(±0.02) and q = 1.9(±0.3). To investigate the tradeoff between γ_0 and q, we further fix q = 1 as a common

assumption, yielding γ_0 =1.53(±0.01). We also fit the *P-V-T* data with a fixed V_0 to 97.76 Å^3 and θ_0 to 631 K alone, yielding K_{T0} = 151(±4) GPa, K_0' = 3.2(±0.2), γ_0 = 1.6(±0.5) and q = 1.3(±0.9), which are in agreement with the first fitting within uncertainties (Table 2). These thermoelastic parameters produce isothermal compression curves (Fig. 5b) consistent with those obtained from HT-BM3 EoS (Fig. 5a). The fitting residuals indicate the discrepancies between measured and calculated pressure are ranging from -1.7 to 1.7 GPa within the investigated pressure and temperature range (Fig. 5b). In summary, both HT-BM3 EoS and MGD EoS results here comprise the first characterization of high-temperature properties of $CaCO_3$-*Pmmn* and can be used to model the chemical and physical properties of $CaCO_3$ in the lower mantle.

Neither of EoS yields a superior or significantly different fit to the experimental data (Fig. 5) and the results for density and bulk sound velocity of $CaCO_3$-*Pmmn* are not significantly affected by the choice of EoS. Calculated densities and velocities follow geotherms from 45 to 80 GPa (Fig. 6 and 7), which does not extrapolate our experimental *P-T* conditions significantly and minimizes the potential errors produced by extrapolation of the thermal equation of state.

Implications

Due to the substantially lower density of carbonates than the principal constituents of the lower mantle (Fig. 6a), sufficient amounts of carbonates may be expected to affect the buoyancy of the subducting slab and its seismic signature, which would be the main manifestations that could be used to constrain the survival and behavior of carbonates subducted into Earth's lower mantle. Calcite/aragonite is one of the most abundant carbonates at shallow depths, along with dolomite ($CaMg(CO_3)_2$) and magnesite ($MgCO_3$) (Luth, 1999). During subduction, $CaMg(CO_3)_2$ breaks down to $MgCO_3$ and $CaCO_3$ above 5 GPa (Luth, 2004). The two end-member carbonates,

$CaCO_3$ and $MgCO_3$, have melting points above typical slab geotherms and thus have been suggested to remain stable in the lower mantle (Li et al., 2017; Solopova et al., 2014; Thomson et al., 2014), where they may be trapped in super-deep diamonds (Brenker et al., 2007; Bulanova et al., 2010; Tschauner et al., 2018). However, as these diamonds provide only samples of local composition that may not be typical of the mantle, geophysical methods may provide useful bounds on the abundance of these carbonates in the deep Earth. Key questions include what maximum amounts of each carbonate or mixture are consistent with observed behaviors and properties of subducting carbonate-bearing slabs in the transition zone and lower mantle.

To understand the dynamics and seismic signatures of subducting carbonate-bearing slabs, density (ρ) and bulk sound velocity (V_Φ) of $CaCO_3$ and $MgCO_3$ at relevant P-T conditions are firstly modeled based on the thermal equations of state. The bulk sound velocity is calculated by $V_\Phi = (K_S/\rho)^{1/2}$, where $K_S = K_{T0}(1+\alpha\gamma T)$, which are determined by HT-BM3 EoS and MGD EoS. Because the thermoelastic parameters of $CaCO_3$-$P2_1/c$-1 have not been constrained experimentally or theoretically, we cannot address the physical properties change due to phase transition from $CaCO_3$-$P2_1/c$-1 to $CaCO_3$-*Pmmn*. We assume the phase transition from $CaCO_3$-*Pnma* to $CaCO_3$-*Pmmn* occurred at 45 GPa. The thermoelastic parameters used in the modeling of $CaCO_3$-*Pnma* (Litasov et al., 2017), $CaCO_3$-*Pmmn* (this study) and magnesite ($MgCO_3$-$R\bar{3}c$) (Litasov et al., 2008) are summarized in Table 2. A cold slab temperature profile [600 K cooler than normal mantle geotherm (Syracuse et al., 2010)] is considered in the model as a typical scenario most likely to retain carbonate minerals during subduction. The calculated ρ and V_Φ of $CaCO_3$ and $MgCO_3$ from 30 to 80 GPa are plotted in Fig. 6, and both HT-BM3 EoS and MGD EoS of $CaCO_3$ and $MgCO_3$ provide similar results. The phase transition of $CaCO_3$-*Pnma* to $CaCO_3$-*Pmmn* in our model leads to an increase in ρ by ~4.5% but a decrease in V_Φ by ~0.8%,

consistent with previous modeled results (Bayarjargal et al., 2018; Litasov et al., 2017). At mid-lower mantle conditions, the density of $CaCO_3$-*Pmmn* is higher than $MgCO_3$-$R\bar{3}c$ by ~10-12%, whereas the V_Φ is lower by ~9-11%. In comparison to surrounding "average" mantle represented by the Preliminary Reference Earth Model (Dziewonski and Anderson, 1981), pure $CaCO_3$ in the lower mantle exhibits V_Φ ~15% lower, while $MgCO_3$ has V_Φ closer to PREM (Fig. 6b). As a result, slow seismic anomalies in the mid-lower mantle may be more likely to be associated with local enrichment in $CaCO_3$ than $MgCO_3$.

More realistically, $CaCO_3$ and $MgCO_3$ are components of carbonated mantle lithologies (Poli and Schmidt, 2002), and the role of these carbonates in changing properties of the subducting slabs may provide a way to estimate bounds on amounts of these carbonates. To determine the physical properties of carbon-bearing rocks in the lower mantle, we must account for geologically relevant mixtures of carbonates with the major mantle silicate and oxide phases (Poli and Schmidt, 2002). It is likely that the carbonate content of subducted rocks varies substantially, from a typical value of ~0.5 mol% for altered oceanic basalts, ranging up to ~10 mol.% due to local enrichment of carbonates (e.g., Alt and Teagle, 1999; Shilobreeva et al., 2011). The basalt part of the subducting slab transforms at lower mantle conditions to a mixture of bridgmanite, Ca-perovskite, stishovite and Al-bearing calcium-ferrite-type (cf-) silicate (Dorfman, 2016). Mixing this assemblage with carbonates will affect not only the chemical behavior of the rock but also its geophysical behavior. We thus model ρ and V_Φ profile of carbonated basalt in the lower mantle from 30 to 80 GPa along a cold slab geotherm (Syracuse et al., 2010) as a typical scenario. Thermoelastic parameters of relevant phases, including constituents of subducted slab (Stixrude and Lithgow-Bertelloni, 2011) and a mixture $CaCO_3$-$MgCO_3$ used in the model are summarized in Table 2. $CaCO_3$ and $MgCO_3$ are added into the

metamorphosed basalt assemblages as a 1:1 molar ratio in proportions of 0 (i.e., eclogite), 2, 5 and 10 mol.%, respectively. The bulk properties of carbonated basalt are calculated based on MGD EoS by using a Hashin-Shtrikman averaging scheme (Cottaar et al., 2014).

The comparison of the bulk sound velocity profile between eclogite and carbonated-eclogite illustrates the effects of carbonate on seismic signatures of the subducting slab. The modeled results show V_Φ of eclogite can be decreased by at most ~2.0 % with the presence of 10 mol.% carbonates in the case of maximum carbonate enrichment and zero loss of carbonate during subduction. Even for this extreme upper bound, the effect of $CaCO_3$ phase transition on the seismic velocity of the slab, increased by ~0.1%, is invisible (Fig. 7a). In the case of typical 0.5 mol.% carbonates presence in the subducting slab, the V_Φ of eclogite would decrease by less than 0.1 %. Comparing to the ambient mantle profile (PREM), the subducting slabs exhibit high V_Φ zones, which cannot be changed by adding carbonates. Therefore, the presence of carbonates in the lower mantle is unlikely to be detected by seismic observation. Previous studies proposed that the presence of sufficient amounts (i.e., 10 mol.%) of carbonates would cause shear velocity discontinuities (decreased by 7%) due to $CaCO_3$-$P2_1$/c-l to $CaCO_3$-*Pmmn* phase transition (Bayarjargal et al., 2018), and largely localized anisotropy due to small shear modulus of $MgCO_3$ (Yao et al., 2018). Although the region with >1% seismic velocity anomaly is detectable by seismic tomography (e.g., French and Romanowicz, 2015), considering the typical concentration and thickness of carbonate depositions on the oceanic crust, even the localized shear velocity anomaly or anisotropy caused by the presence of carbonates is unlikely detectable due to the limit of spatial resolution of seismic tomography.

The ρ contrast between carbonates and surrounding phases at lower mantle conditions is a source of buoyancy that impedes the downward motion of the slab. In comparison to the average

mantle density profile (PREM), eclogite is denser than the ambient lower mantle by ~0.8 %, indicating the higher density of eclogite helps drive subduction in the lower mantle. However, the model results indicate the density of highly carbonated eclogite with maximum carbonate enrichment 10 mol.% carbonates are lower than the ambient lower mantle by ~0.6 % (Fig. 7b), and thus will not sink. The maximum amount of carbonate stored in eclogite that will not contribute to slab stagnation is 5 mol.%. This is also much greater than the typical 0.5% carbonate content in altered oceanic crust. The temperature effects on the density of subducting slab are negligible, i.e., the calculated density of eclogite decreases by ~1% when changing the reference geotherm from cold slab to hot slab [300 K cooler than normal mantle geotherm (Syracuse et al., 2010)]. In addition, the buoyancy of carbonates is not expected to significantly affect the dynamics of subducting slabs relative to other metastable components of cold slabs potentially present in far greater abundance, particularly metastable olivine (Rubie and Ross, 1994) and pyroxene (van Mierlo et al., 2013).

Thermoelastic properties of $CaCO_3$-*Pmmn* provide useful geochemical constraints necessary for modeling the phase equilibria of carbonates with mantle phases at lower mantle conditions. Reactions that control the presence of $CaCO_3$ in the slab include melting, decarbonation and redox interactions with ambient mantle phases. For example, recent experimental studies suggest the $CaCO_3$ decarbonation occurs in the presence of silica at lower mantle conditions forming Ca-perovskite and CO_2 (Drewitt et al., 2019; Li et al., 2018), and the redox reaction between $CaCO_3$ and metallic iron in the ambient mantle is proposed to be a mechanism of deep diamond formation (Martirosyan et al., 2016; Palyanov et al., 2013). The *P*-*T* boundaries of both reactions are essential to understanding the fate of subducted $CaCO_3$ and equilibrium between $CaCO_3$ and mantle phases. However, both boundaries are not well

constrained by experiments, mainly due to the kinetic barriers in reactions and uncertainties in pressure and temperature measurements. For other lower mantle phases, thermodynamic modeling has begun to be used to construct physically-consistent phase diagrams (e.g., Stixrude and Lithgow-Bertelloni, 2011). The newly determined thermoelastic parameters of $CaCO_3$-*Pmmn* combined with those of other mantle phases will contribute to more quantitative constraints on phase equilibria in the carbonate-silicate system at lower mantle conditions.

Acknowledgments

We acknowledge the editor for handling our manuscript, and two anonymous reviewers for their constructive and thoughtful feedback. This work was supported by NSF grant (EAR-1751664), and startup fund to S.M.D. GeoSoilEnviroCARS is supported by the NSF-Earth Sciences (EAR-1634415) and DOE-GeoSciences (DE-FG02-94ER14466). Use of the COMPRES-GSECARS gas loading system was supported by COMPRES under NSF Cooperative Agreement EAR-1606856 and by GSECARS through NSF grant EAR-1634415 and DOE grant DE-FG02-94ER14466. This research used resources of the Advanced Photon Source, a U.S. Department of Energy (DOE) Office of Science User Facility operated for the DOE Office of Science by Argonne National Laboratory under Contract No. DE-AC02-06CH11357.

References

Alt, J.C., and Teagle, D.A.H. (1999) The uptake of carbon during alteration of ocean crust. Geochimica et Cosmochimica Acta, 63(10), 1527-1535.

Angel, R.J. (2000) Equations of state. High-Temperature and High-Pressure Crystal Chemistry, 41(1), 35-59.

Bayarjargal, L., Fruhner, C.J., Schrodt, N., and Winkler, B. (2018) $CaCO_3$ phase diagram studied with Raman spectroscopy at pressures up to 50 GPa and high temperatures and DFT modeling. Physics of the Earth and Planetary Interiors, 281, 31-45.

Biellmann, C., Gillet, P., Peyronneau, J., and Reynard, B. (1993) Experimental evidence for carbonate stability in the Earth's lower mantle. Earth and Planetary Science Letters, 118(1-4), 31-41.

Birch, F. (1952) Elasticity and constitution of the Earth's interior. Journal of Geophysical Research, 57(2), 227-286.

Brenker, F.E., Vollmer, C., Vincze, L., Vekemans, B., Szymanski, A., Janssens, K., Szaloki, I., Nasdala, L., Joswig, W., and Kaminsky, F. (2007) Carbonates from the lower part of transition zone or even the lower mantle. Earth and Planetary Science Letters, 260(1-2), 1-9.

Brown, J.M., and Shankland, T.J. (1981) Thermodynamic Parameters in the Earth as Determined from Seismic Profiles. Geophysical Journal of the Royal Astronomical Society, 66(3), 579-596.

Bulanova, G.P., Walter, M.J., Smith, C.B., Kohn, S.C., Armstrong, L.S., Blundy, J., and Gobbo, L. (2010) Mineral inclusions in sublithospheric diamonds from Collier 4 kimberlite pipe, Juina, Brazil: subducted protoliths, carbonated melts and primary kimberlite magmatism. Contributions to Mineralogy and Petrology, 160(4), 489-510.

Cottaar, S., Heister, T., Rose, I., and Unterborn, C. (2014) BurnMan: A lower mantle mineral physics toolkit. Geochemistry Geophysics Geosystems, 15(4), 1164-1179.

Dasgupta, R., and Hirschmann, M.M. (2006) Melting in the Earth's deep upper mantle caused by carbon dioxide. Nature, 440(7084), 659-62.

-. (2010) The deep carbon cycle and melting in Earth's interior. Earth and Planetary Science Letters, 298(1-2), 1-13.

Dorfman, S.M. (2016) Phase Diagrams and Thermodynamics of Lower Mantle Materials. Deep Earth: Physics and Chemistry of the Lower Mantle and Core, 217, 241-252.

Dorfman, S.M., Badro, J., Nabiei, F., Prakapenka, V.B., Cantoni, M., and Gillet, P. (2018) Carbonate stability in the reduced lower mantle. Earth and Planetary Science Letters, 489, 84-91.

Drewitt, J.W.E., Walter, M.J., Zhang, H.L., McMahon, S.C., Edwards, D., Heinen, B.J., Lord, O.T., Anzellini, S., and Kleppe, A.K. (2019) The fate of carbonate in oceanic crust subducted into earth's lower mantle. Earth and Planetary Science Letters, 511, 213-222.

Dziewonski, A.M., and Anderson, D.L. (1981) Preliminary Reference Earth Model. Physics of the Earth and Planetary Interiors, 25(4), 297-356.

Fabrichnaya, O., Saxena, S.K., Richet, P., and Westrum, E.F. (2004) Thermodynamic data, models, and phase diagrams in multicomponent oxide systems: an assessment for materials and planetary scientists based on calorimetric, volumetric and phase equilibrium data. Springer Science & Business Media.

Fei, Y. (1995) Thermal expansion. Mineral physics and crystallography: a handbook of physical constants, 2, 29-44.

Fei, Y., Ricolleau, A., Frank, M., Mibe, K., Shen, G., and Prakapenka, V. (2007) Toward an internally consistent pressure scale. Proceedings of the National Academy of Sciences, 104(22), 9182-6.

French, S.W., and Romanowicz, B. (2015) Broad plumes rooted at the base of the Earth's mantle beneath major hotspots. Nature, 525(7567), 95-9.

Gavryushkin, P.N., Martirosyan, N.S., Inerbaev, T.M., Popov, Z.I., Rashchenko, S.V., Likhacheva, A.Y., Lobanov, S.S., Goncharov, A.F., Prakapenka, V.B., and Litasov, K.D.

(2017) Aragonite-II and $CaCO_3$-VII: New High-Pressure, High-Temperature Polymorphs of $CaCO_3$. Crystal Growth & Design, 17(12), 6291-6296.

Ghosh, S., Litasov, K., and Ohtani, E. (2014) Phase relations and melting of carbonated peridotite between 10 and 20 GPa: a proxy for alkali- and CO_2-rich silicate melts in the deep mantle. Contributions to Mineralogy and Petrology, 167(2), 23.

Jackson, I. (1998) Elasticity, composition and temperature of the Earth's lower mantle: a reappraisal. Geophysical Journal International, 134(1), 291-311.

Jackson, I., and Rigden, S.M. (1996) Analysis of *P-V-T* data: Constraints on the thermoelastic properties of high-pressure minerals. Physics of the Earth and Planetary Interiors, 96(2-3), 85-112.

Kelemen, P.B., and Manning, C.E. (2015) Reevaluating carbon fluxes in subduction zones, what goes down, mostly comes up. Proceedings of the National Academy of Sciences, 112(30), E3997-4006.

Kiseeva, E.S., Litasov, K.D., Yaxley, G.M., Ohtani, E., and Kamenetsky, V.S. (2013) Melting and Phase Relations of Carbonated Eclogite at 9-21 GPa and the Petrogenesis of Alkali-Rich Melts in the Deep Mantle. Journal of Petrology, 54(8), 1555-1583.

Le Bail, A., Duroy, H., and Fourquet, J. (1988) Ab-initio structure determination of $LiSbWO_6$ by X-ray powder diffraction. Materials Research Bulletin, 23(3), 447-452.

Li, X.Y., Zhang, Z.G., Lin, J.F., Ni, H.W., Prakapenka, V.B., and Mao, Z. (2018) New High-Pressure Phase of $CaCO_3$ at the Topmost Lower Mantle: Implication for the Deep-Mantle Carbon Transportation. Geophysical Research Letters, 45(3), 1355-1360.

Li, Y., Zou, Y.T., Chen, T., Wang, X.B., Qi, X.T., Chen, H.Y., Du, J.G., and Li, B.S. (2015) *P-V-T* equation of state and high-pressure behavior of $CaCO_3$ aragonite. American Mineralogist, 100(10), 2323-2329.

Li, Z.Y., Li, J., Lange, R., Liu, J.C., and Mintzer, B. (2017) Determination of calcium carbonate and sodium carbonate melting curves up to Earth's transition zone pressures with implications for the deep carbon cycle. Earth and Planetary Science Letters, 457, 395-402.

Litasov, K.D., Fei, Y., Ohtani, E., Kuribayashi, T., and Funakoshi, K. (2008) Thermal equation of state of magnesite to 32GPa and 2073K. Physics of the Earth and Planetary Interiors, 168(3-4), 191-203.

Litasov, K.D., Shatskiy, A., Gavryushkin, P.N., Bekhtenova, A.E., Dorogokupets, P.I., Danilov, B.S., Higo, Y., Akilbekov, A.T., and Inerbaev, T.M. (2017) *P-V-T* equation of state of $CaCO_3$ aragonite to 29 GPa and 1673 K: In situ X-ray diffraction study. Physics of the Earth and Planetary Interiors, 265, 82-91.

Lobanov, S.S., Dong, X., Martirosyan, N.S., Samtsevich, A.I., Stevanovic, V., Gavryushkin, P.N., Litasov, K.D., Greenberg, E., Prakapenka, V.B., Oganov, A.R., and Goncharov, A.F. (2017) Raman spectroscopy and X-ray diffraction of sp^3 $CaCO_3$ at lower mantle pressures. Physical Review B, 96(10), 104101.

Luth, R.W. (1999) Carbon and carbonates in the mantle. Mantle Petrology: Field Observations and High Pressure Experimentation: A Tribute to Francis R (Joe) Boyd, 6, 297-316.

Luth, R.W. (2004) Experimental determination of the reaction aragonite + magnesite = dolomite at 5 to 9 GPa. Contributions to Mineralogy and Petrology, 141(2), 222-232.

Marcondes, M.L., Justo, J.F., and Assali, L.V.C. (2016) Carbonates at high pressures: Possible carriers for deep carbon reservoirs in the Earth's lower mantle. Physical Review B.

Martirosyan, N.S., Yoshino, T., Shatskiy, A., Chanyshev, A.D., and Litasov, K.D. (2016) The $CaCO_3$–Fe interaction: Kinetic approach for carbonate subduction to the deep Earth's mantle. Physics of the Earth and Planetary Interiors, 259, 1-9.

Oganov, A.R., Glass, C.W., and Ono, S. (2006) High-pressure phases of $CaCO_3$: Crystal structure prediction and experiment. Earth and Planetary Science Letters, 241(1-2), 95-103.

Oganov, A.R., Ono, S., Ma, Y.M., Glass, C.W., and Garcia, A. (2008) Novel high-pressure structures of $MgCO_3$, $CaCO_3$ and CO_2 and their role in Earth's lower mantle. Earth and Planetary Science Letters, 273(1-2), 38-47.

Ono, S., Kikegawa, T., and Ohishi, Y. (2007) High-pressure transition of $CaCO_3$. American Mineralogist, 92(7), 1246-1249.

Ono, S., Kikegawa, T., Ohishi, Y., and Tsuchiya, J. (2005) Post-aragonite phase transformation in $CaCO_3$ at 40 GPa. American Mineralogist, 90(4), 667-671.

Palaich, S.E.M., Heffern, R.A., Hanfland, M., Lausi, A., Kavner, A., Manning, C.E., and Merlini, M. (2016) High-pressure compressibility and thermal expansion of aragonite. American Mineralogist, 101(7-8), 1651-1658.

Palyanov, Y.N., Bataleva, Y.V., Sokol, A.G., Borzdov, Y.M., Kupriyanov, I.N., Reutsky, V.N., and Sobolev, N.V. (2013) Mantle-slab interaction and redox mechanism of diamond formation. Proceedings of the National Academy of Sciences, 110(51), 20408-13.

Pickard, C.J., and Needs, R.J. (2015) Structures and stability of calcium and magnesium carbonates at mantle pressures. Physical Review B, 91(10).

Poirier, J.-P. (2000) Introduction to the Physics of the Earth's Interior. Cambridge University Press.

Poli, S., and Schmidt, M.W. (2002) Petrology of subducted slabs. Annual Review of Earth and Planetary Sciences, 30(1), 207-235.

Prakapenka, V.B., Kubo, A., Kuznetsov, A., Laskin, A., Shkurikhin, O., Dera, P., Rivers, M.L., and Sutton, S.R. (2008) Advanced flat top laser heating system for high pressure research at GSECARS: application to the melting behavior of germanium. High Pressure Research, 28(3), 225-235.

Prescher, C., and Prakapenka, V.B. (2015) DIOPTAS: a program for reduction of two-dimensional X-ray diffraction data and data exploration. High Pressure Research, 35(3), 223-230.

Rivers, M., Prakapenka, V.B., Kubo, A., Pullins, C., Holl, C.M., and Jacobsen, S.D. (2008) The COMPRES/GSECARS gas-loading system for diamond anvil cells at the Advanced Photon Source. High Pressure Research, 28(3), 273-292.

Rohrbach, A., and Schmidt, M.W. (2011) Redox freezing and melting in the Earth's deep mantle resulting from carbon-iron redox coupling. Nature, 472(7342), 209-12.

Rubie, D.C., and Ross, C.R. (1994) Kinetics of the Olivine-Spinel Transformation in Subducting Lithosphere - Experimental Constraints and Implications for Deep Slab Processes. Physics of the Earth and Planetary Interiors, 86(1-3), 223-241.

Seto, Y., Hamane, D., Nagai, T., and Fujino, K. (2008) Fate of carbonates within oceanic plates subducted to the lower mantle, and a possible mechanism of diamond formation. Physics and Chemistry of Minerals, 35(4), 223-229.

Seto, Y., Nishio-Hamane, D., Nagai, T., and Sata, N. (2010) Development of a Software Suite on X-ray Diffraction Experiments. The Review of High Pressure Science and Technology, 20(3), 269-276.

Shilobreeva, S., Martinez, I., Busigny, V., Agrinier, P., and Laverne, C. (2011) Insights into C and H storage in the altered oceanic crust: Results from ODP/IODP Hole 1256D. Geochimica et Cosmochimica Acta, 75(9), 2237-2255.

Smith, D., Lawler, K.V., Martinez-Canales, M., Daykin, A.W., Fussell, Z., Smith, G.A., Childs, C., Smith, J.S., Pickard, C.J., and Salamat, A. (2018) Postaragonite phases of $CaCO_3$ at lower mantle pressures. Physical Review Materials, 2(1).

Solopova, N.A., Dubrovinsky, L., Spivak, A.V., Litvin, Y.A., and Dubrovinskaia, N. (2014) Melting and decomposition of $MgCO_3$ at pressures up to 84 GPa. Physics and Chemistry of Minerals, 42(1), 73-81.

Staudigel, H. (2014) Chemical Fluxes from Hydrothermal Alteration of the Oceanic Crust. Treatise on Geochemistry, p. 583-606.

Stixrude, L., and Lithgow-Bertelloni, C. (2011) Thermodynamics of mantle minerals - II. Phase equilibria. Geophysical Journal International, 184(3), 1180-1213.

Syracuse, E.M., van Keken, P.E., and Abers, G.A. (2010) The global range of subduction zone thermal models. Physics of the Earth and Planetary Interiors, 183(1-2), 73-90.

Thomson, A.R., Walter, M.J., Kohn, S.C., and Brooker, R.A. (2016) Slab melting as a barrier to deep carbon subduction. Nature, 529(7584), 76-9.

Thomson, A.R., Walter, M.J., Lord, O.T., and Kohn, S.C. (2014) Experimental determination of melting in the systems enstatite-magnesite and magnesite-calcite from 15 to 80 GPa. American Mineralogist, 99(8-9), 1544-1554.

Toby, B.H. (2001) EXPGUI, a graphical user interface for GSAS. Journal of Applied Crystallography, 34(2), 210-213.

Tschauner, O., Huang, S., Greenberg, E., Prakapenka, V., Ma, C., Rossman, G., Shen, A., Zhang, D., Newville, M., and Lanzirotti, A. (2018) Ice-VII inclusions in diamonds: Evidence for aqueous fluid in Earth's deep mantle. Science, 359(6380), 1136-1139.

van Mierlo, W.L., Langenhorst, F., Frost, D.J., and Rubie, D.C. (2013) Stagnation of subducting slabs in the transition zone due to slow diffusion in majoritic garnet. Nature Geoscience, 6(5), 400-403.

Yao, C., Wu, Z.Q., Zou, F., and Sun, W.D. (2018) Thermodynamic and Elastic Properties of Magnesite at Mantle Conditions: First-Principles Calculations. Geochemistry Geophysics Geosystems, 19(8), 2719-2731.

Ye, Y., Smyth, J.R., and Boni, P. (2012) Crystal structure and thermal expansion of aragonite-group carbonates by single-crystal X-ray diffraction. American Mineralogist, 97(4), 707-712.

Zhang, Z.G., Mao, Z., Liu, X., Zhang, Y.G., and Brodholt, J. (2018) Stability and Reactions of $CaCO_3$ Polymorphs in the Earth's Deep Mantle. Journal of Geophysical Research-Solid Earth, 123(8), 6491-6500.

Zhu, F., Li, J., Liu, J.C., Lai, X.J., Chen, B., and Meng, Y. (2019) Kinetic Control on the Depth Distribution of Superdeep Diamonds. Geophysical Research Letters, 46(4), 1984-1992.

Figure captions

Figure 1: Full-profile Le Bail refinement confirms the synthesis of $CaCO_3$-*Pmmn*. Measured XRD data for the quenched sample after heating at 49 GPa and 300 K (black dots) are consistent with orthorhombic post-aragonite structure (space group *Pmmn* with Z = 2) (black ticks below). Le Bail fit (red curve) also includes expected peak positions for Au calibrant (yellow sticks) and Ne medium (blue ticks). One unknown peak at 2θ around ~7° (marked by an asterisk) may be from the metastable $CaCO_3$-$P2_1$/c-l due to kinetics. The wavelength of the monochromatic X-ray beam is 0.3344 Å.

Figure 2: (a) Representative in-situ X-ray diffraction patterns of $CaCO_3$-*Pmmn* measured at high pressures and room temperature (black marker). **(b)** Representative high-temperature X-ray diffraction patterns of $CaCO_3$-*Pmmn* at ~60 GPa (black marker) measured in-situ in a laser-heated diamond anvil cell. In all XRD patterns, Au was used as the internal pressure calibrant (Fei et al., 2007) and laser-absorber (orange marker), while Ne was used as the thermal insulator and pressure medium (blue marker). The wavelength of the monochromatic X-ray beam is 0.3344 Å.

Figure 3: (a) Pressure-volume data for $CaCO_3$-*Pmmn* at room temperature from this study (black circle) and previous studies. Data from Ono et al. (2005) (red square) and Lobanov et al. (2017) (blue square) were recalculated using Pt pressure scale (Fei et al., 2007). Black solid curve (this study) is modeled by BM3 EoS using K_{T0} = 162(±62) GPa, K_0' = 3.1 (±1.1), and V_0 = 96.6(±4.8) Å^3. A brown dashed curve (Oganov et al., 2006) and a purple dashed curve (Marcondes et al., 2016) modeled by BM3 EoS constrained via DFT-GGA and LDA,

respectively. **(b)** Isothermal bulk modulus (K_T) at 300 K calculated by BM3 EoS. The black solid line, dashed line and short-dashed line represent the BM3 EoS fittings without constraint, with a fixed V_0 = 97.76 Å^3 and with reference pressure set at 50 GPa.

Figure 4: Volume Eulerian strain (*f*) - normalized pressure (*F*) plot of $CaCO_3$-*Pmmn*. The dashed line represents the linear fit through the data, and a red envelope indicates 95% confidence interval. The V_0 was set as 96.6 Å^3 obtained by BM3 EoS fitting of experimental data at 300 K.

Figure 5: Measured pressure-volume-temperature data for $CaCO_3$-*Pmmn*. Colorful curves are isotherms at 1300, 1600, 1900, 2200 K modeled by **(a)** HT-BM3 EoS and **(b)** MGD EoS, respectively, with parameters listed in Table 2. Black points and curve are at 300 K same as Fig.3. The lower panel of each figure shows fitting residuals.

Figure 6: Modeled **(a)** density and **(b)** bulk sound velocity profiles of $CaCO_3$ and $MgCO_3$ from 30 to 80 GPa along mantle geotherm (Brown and Shankland, 1981) compared to PREM model (Dziewonski and Anderson, 1981) and eclogite (assumed to be composed by 27 mol.% bridgmanite [$(Mg_{0.9},Fe_{0.1})SiO_3$], 24 mol.% Ca-perovskite ($CaSiO_3$), 20 mol.% stishovite (SiO_2), 29 mol.% Al-bearing calcium-ferrite-type silicate [$(Mg_{0.9},Fe_{0.1})Al_2O_4$]), using the thermoelastic parameters listed in Table 2. In order to clearly illustrate the density contrast of different carbonates, the phase transition of $CaCO_3$-*Pnma* to $CaCO_3$-*Pmmn* is assumed to occur at 45 GPa.

Figure 7: Modeled **(a)** bulk sound velocity and **(b)** density profiles of eclogite and carbonated-eclogite with the presence of $CaCO_3$-$MgCO_3$ mixture as 2, 5 and 10 mol.%, respectively. The eclogite is assumed to be composed by 27 mol.% bridgmanite [$(Mg_{0.9},Fe_{0.1})SiO_3$], 24 mol.% Ca-perovskite ($CaSiO_3$), 20 mol.% stishovite (SiO_2), 29 mol.% Al-bearing calcium-ferrite-type silicate [$(Mg_{0.9},Fe_{0.1})Al_2O_4$], and the thermoelastic parameters of these phases are listed in Table 2. The pressure is ranging from 30 to 80 GPa along cold geotherm (Syracuse et al., 2010). The $CaCO_3$-*Pnma* to $CaCO_3$-*Pmmn* transition is assumed to occur at 45 GPa. The PREM model (Dziewonski and Anderson, 1981) is plotted as a comparison of the averaged mantle.

Table 1. Comparison of parameters of BM3 EoS of $CaCO_3$-*Pmmn* at 300 K

V_0 (Å^3)	K_{T0} (GPa)	K_0'	Method	References
99.4(20)	118(14)	4 (fixed)	XRD (PM[2]: NaCl)	Ono et al. (2005)[3]
97.3(16)	135(12)	4 (fixed)	XRD (No PM)	Lobanov et al. (2017)[3]
109.74	65.4	4.94	DFT-GGA[4]	Oganov et al. (2006)
97.76	122	3.732	DFT-LDA[4]	Marcondes et al. (2016)
96.6(48)	162(62)	3.1(11)	XRD (PM: Ne)[5]	This study
97.76 (fixed)	146.7(19)	3.4(1)	XRD (PM: Ne)[5]	This study

[1] Numbers in parentheses are uncertainties on the last digits.

[2] PM: pressure medium

[3] Refitted by the pressure scale of Pt (Fei et al., 2007).

[4] Results are from 0 K.

[5] Using the pressure scale of Au (Fei et al., 2007).

Table 2. Thermoelastic parameters of $CaCO_3$, $MgCO_3$, and major components in eclogite

Sample	V_0 (Å^3)	K_{T0} (GPa)	K_0'	$\partial K_T/\partial T$ (GPa·K^{-1})	a_0 (10^{-5}K^{-1})	a_1 (10^{-8}K^{-2})	θ_0 (K)	γ_0	q
$CaCO_3$-*Pmmn*[1]	97.76[5]	146.7(19)[5]	3.4(1)[5]	-0.021(1)	4.3(3)	0.8(2)	631[5]	1.94(2)	1.9(3)
$CaCO_3$-*Pmmn*[1]	97.76[5]	146(5)	3.4(2)	-0.022(8)	4.4(5)	0.9(8)	-	-	-
$CaCO_3$-*Pmmn*[1]	97.76[5]	151(4)	3.2(2)	-	-	-	631[5]	1.6(5)	1.3(9)
$CaCO_3$-*Pmmn*[1]	97.76[5]	146.7(19)[5]	3.4(1)[5]	-	-	-	631[5]	1.53(1)	1[5]
$CaCO_3$-*Pnma*[2]	227.11(3)[6]	67.0(8)	4.74(12)	-0.016(1)	4.95(22)	2.77(40)	516[5]	1.39(1)	1[5]
$MgCO_3$-$R\bar{3}c$[3]	279.55(2)	97.1(5)	5.44(7)	-0.013(1)	4.03(7)	0.49(10)	747[5]	1.38(1)	1[5]
$MgSiO_3$ (perovskite)[4]	162.40	251(3)	4.1(1)				905(5)	1.57(5)	1.1(3)
$FeSiO_3$ (perovskite)[4]	169.31	272(40)	4.1(10)				871(26)	1.57(30)	1.1(10)
$MgAl_2O_4$ (cf)[4]	480.63	211(1)	4.1(1)				838(16)	1.31(30)	1.0(10)
$FeAl_2O_4$ (cf)[4]	494.97	211 (10)	4.1(10)				804(69)	1.31(30)	1.0(10)
$CaSiO_3$ (perovskite)[4]	45.58	236 (4)	3.9 (2)				796 (44)	1.89 (7)	0.9 (16)
SiO_2 (stishovite)[4]	46.56	314(8)	3.8(1)				1108(13)	1.37(17)	2.8(22)

[1] This study.

[2] Litasov et al. (2017).

[3] Litasov et al. (2008).

[4] Stixrude and Lithgow-Bertelloni (2011).

[5] Fixed during fitting.

[6] Numbers in parentheses are uncertainties on the last digits

Figure 1

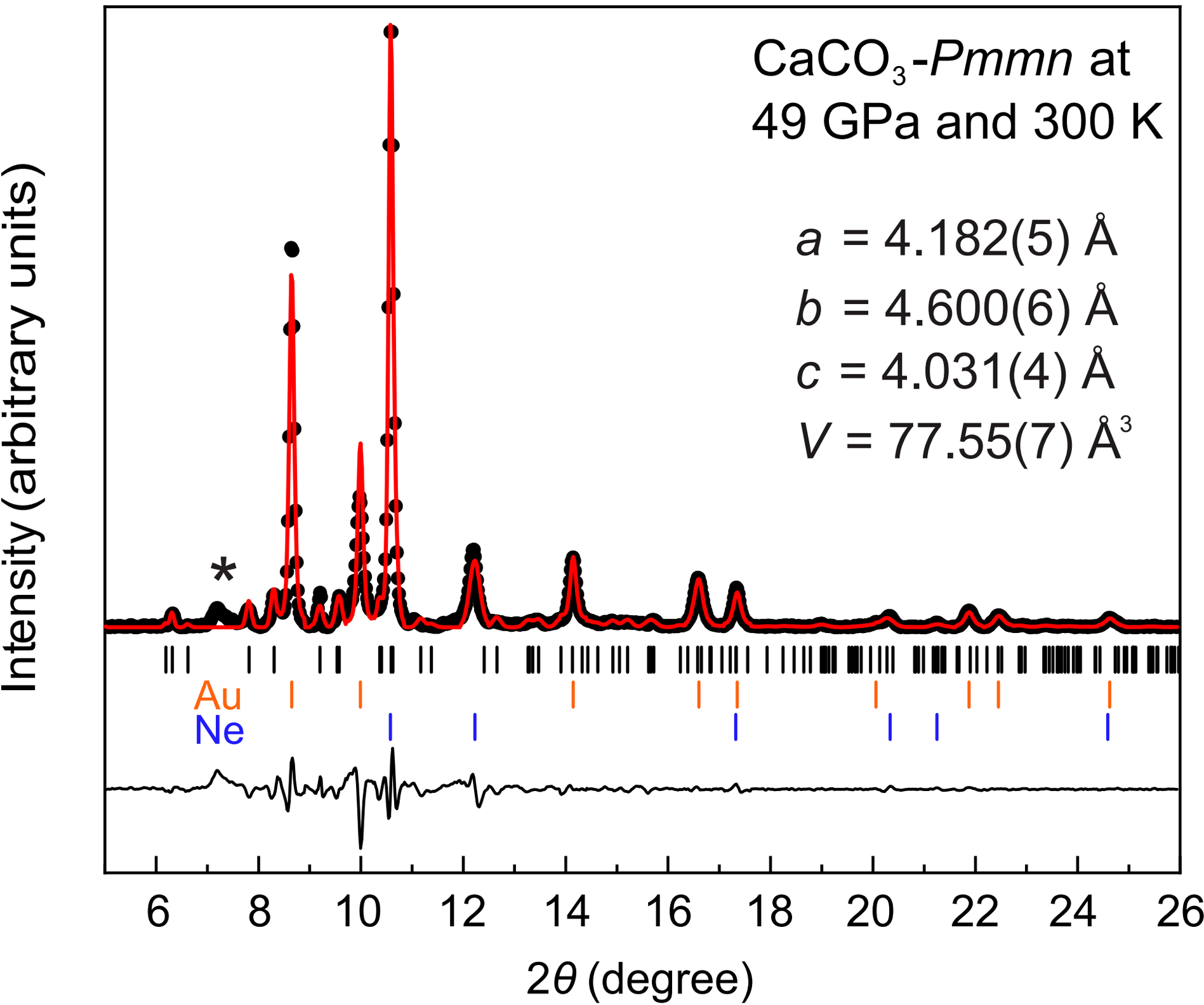
CaCO3-Pmmn at
49 GPa and 300 K
a = 4.182(5) Å
b = 4.600(6) Å
c = 4.031(4) Å
V = 77.55(7) Å3
*
Au
Ne
Intensity (arbitrary units)
6
8
10
12
14
16
18
20
22
24
26
2θ (degree)

Figure 2(a)

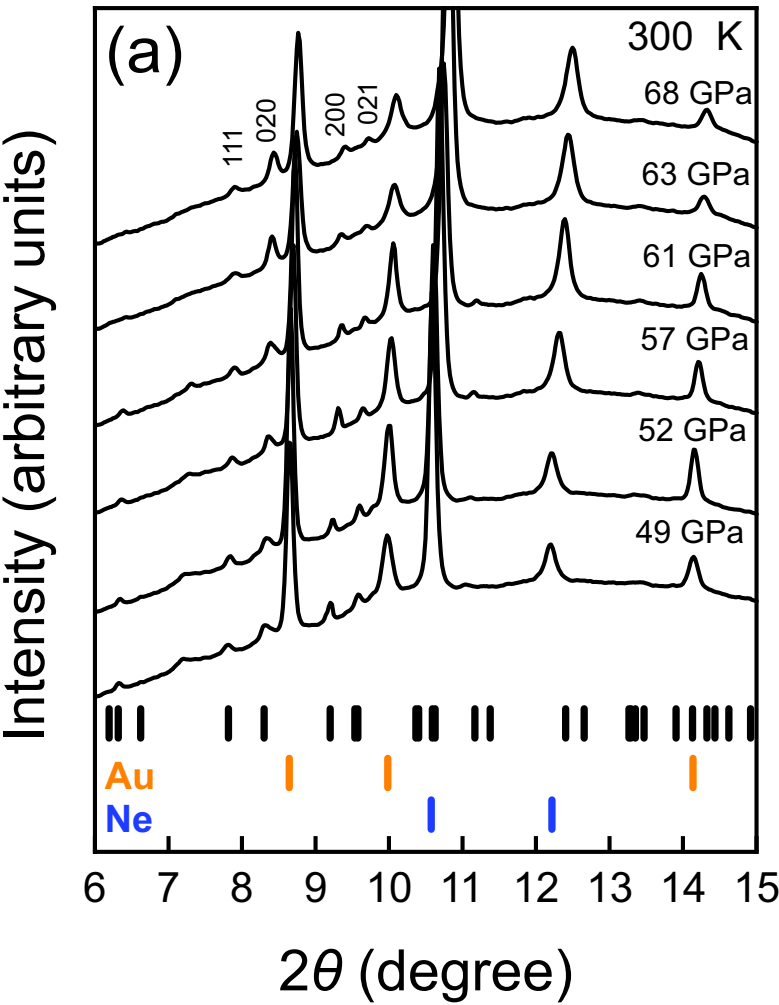
(a)
300 K
68 GPa
63 GPa
61 GPa
57 GPa
52 GPa
49 GPa
111
020
200
021
Au
Ne
Intensity (arbitrary units)
6
7
8
9
10
11
12
13
14
15
2θ (degree)

Figure 2(b)

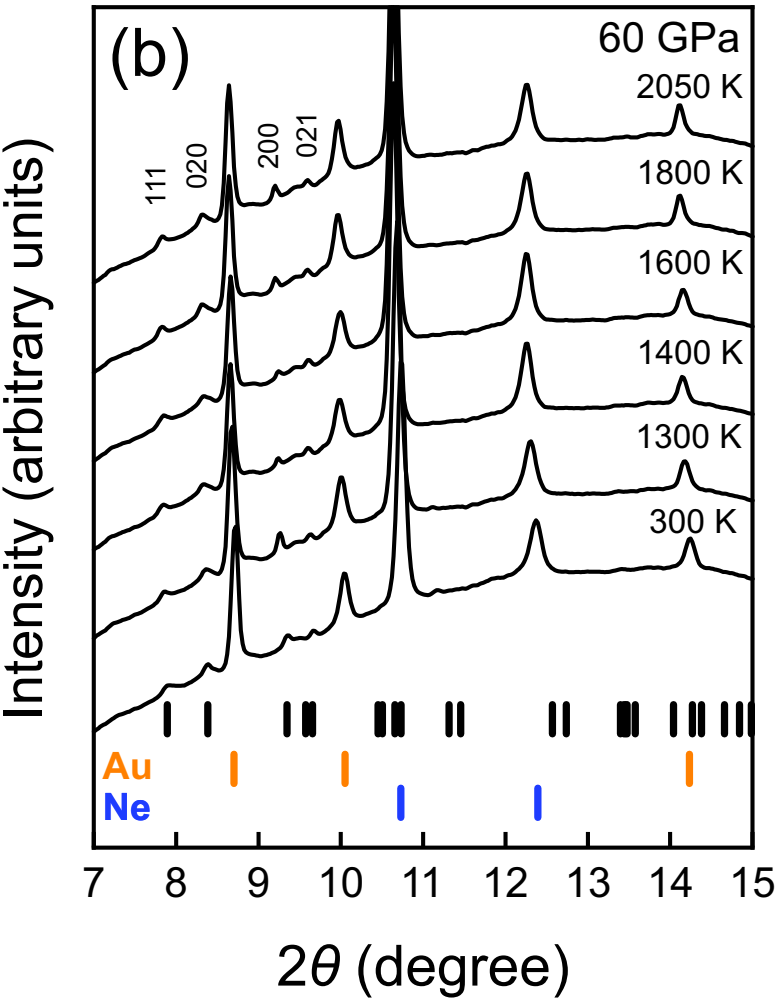
(b)
60 GPa
2050 K
1800 K
1600 K
1400 K
1300 K
300 K
111
020
200
021
Au
Ne
Intensity (arbitrary units)
7
8
9
10
11
12
13
14
15
2θ (degree)

Figure 3(a)

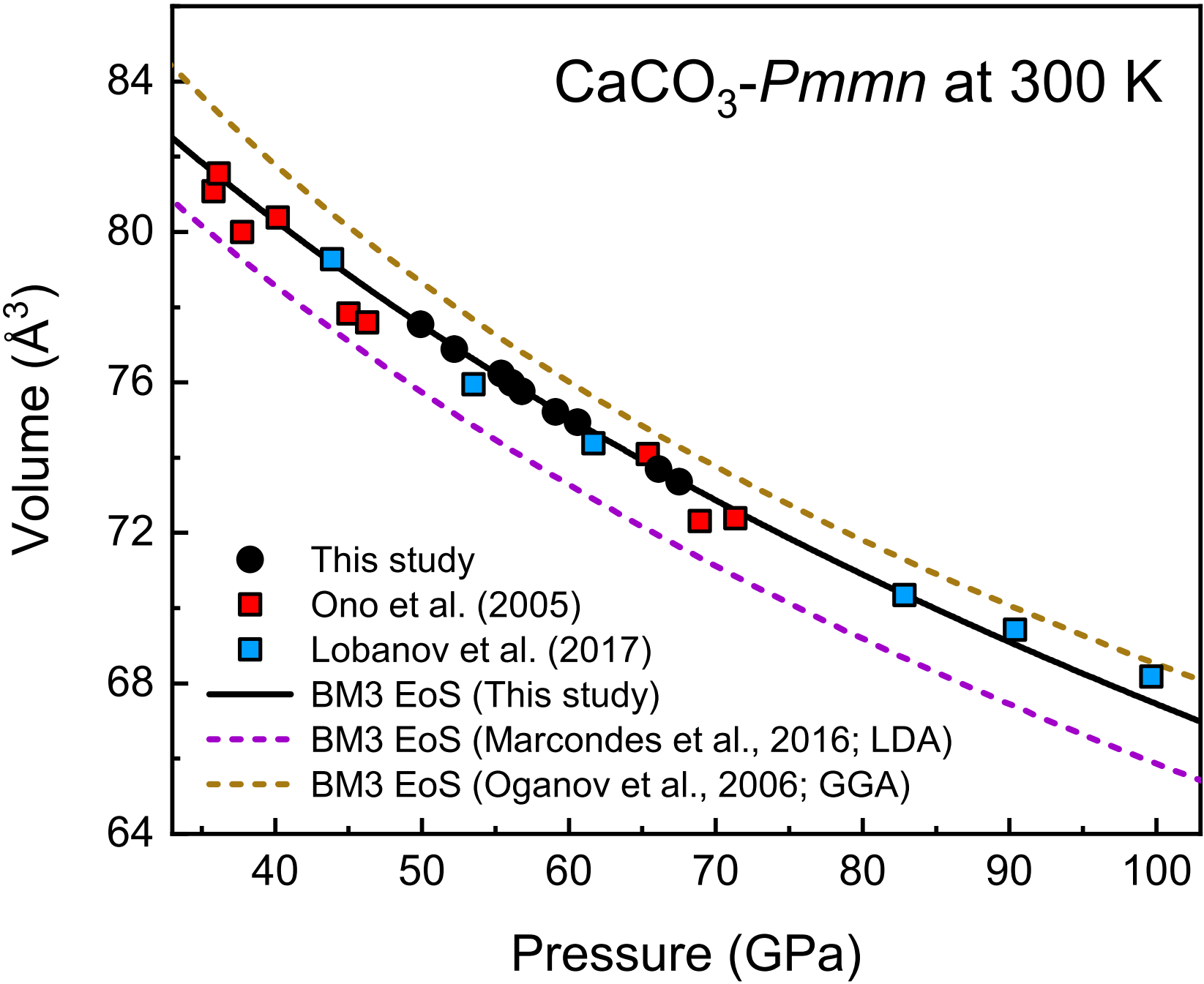
CaCO3-Pmmn at 300 K
Volume (Å3)
Pressure (GPa)
84
80
76
72
68
64
40
50
60
70
80
90
100
This study
Ono et al. (2005)
Lobanov et al. (2017)
BM3 EoS (This study)
BM3 EoS (Marcondes et al., 2016; LDA)
BM3 EoS (Oganov et al., 2006; GGA)

Figure 3(b)

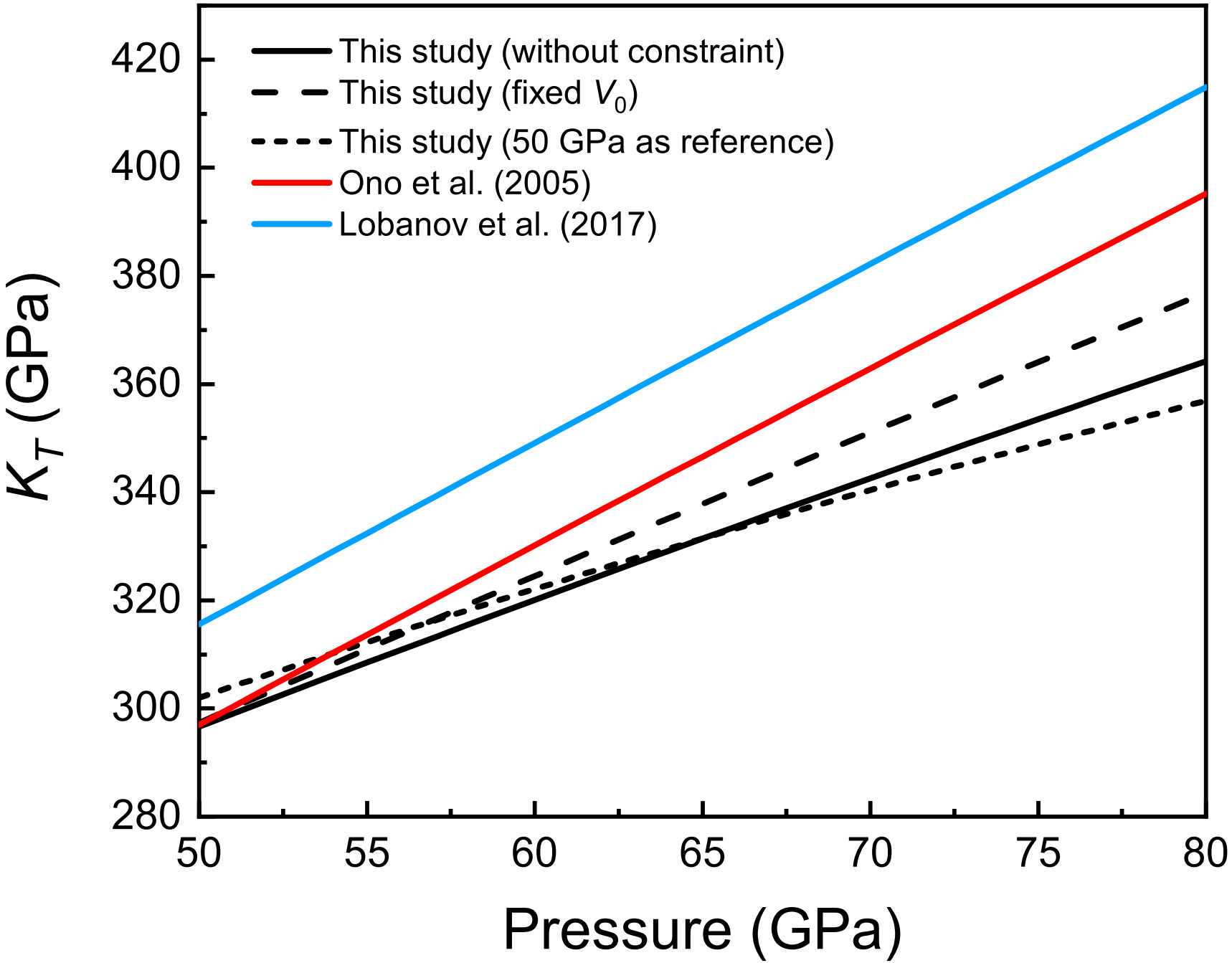
This study (without constraint)
This study (fixed V_0)
This study (50 GPa as reference)
Ono et al. (2005)
Lobanov et al. (2017)
K_T (GPa)
420
400
380
360
340
320
300
280
50
55
60
65
70
75
80
Pressure (GPa)

Figure 4

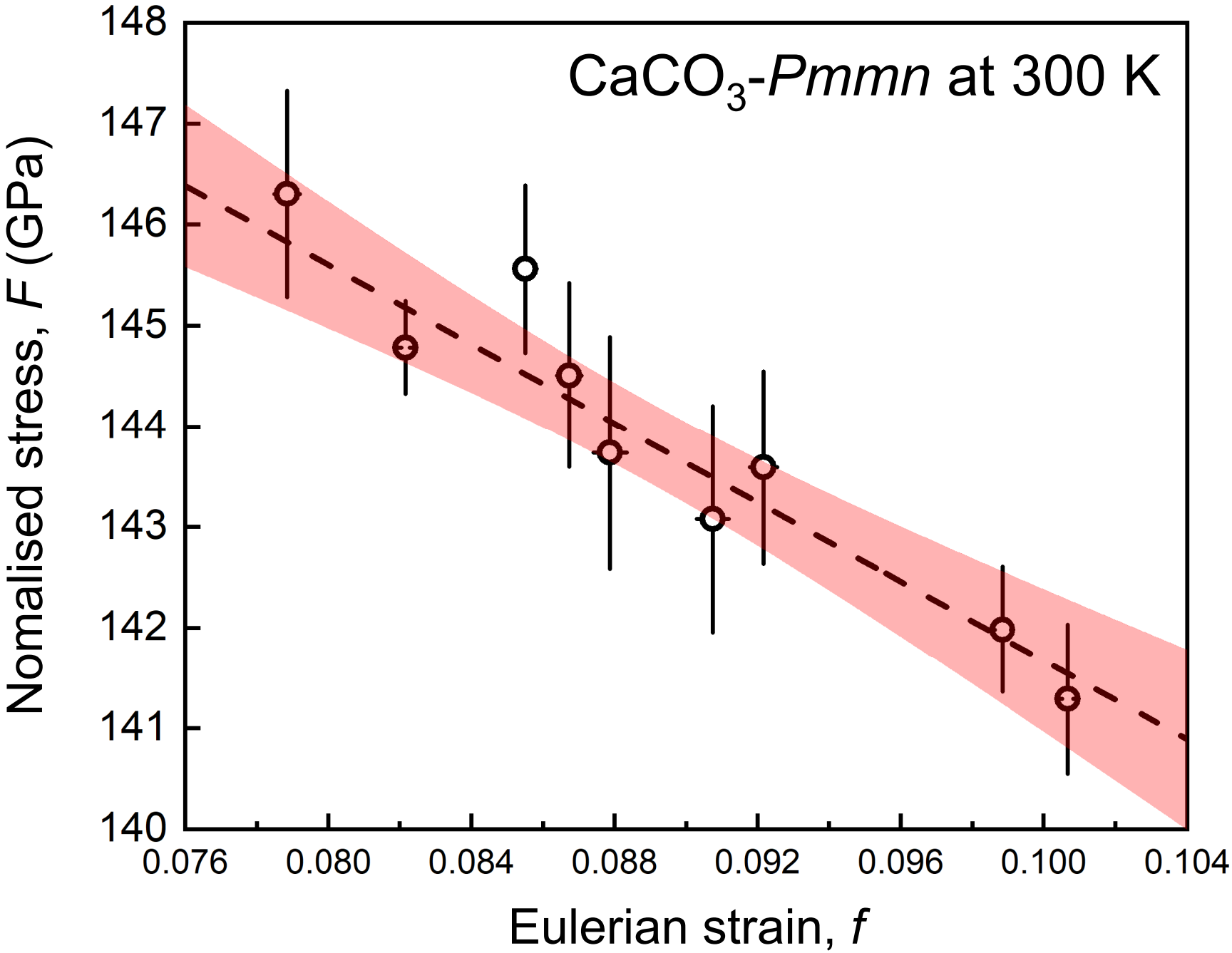
CaCO3-Pmmn at 300 K
Nomalised stress, F (GPa)
Eulerian strain, f
148
147
146
145
144
143
142
141
140
0.076
0.080
0.084
0.088
0.092
0.096
0.100
0.104

Figure 5(a)

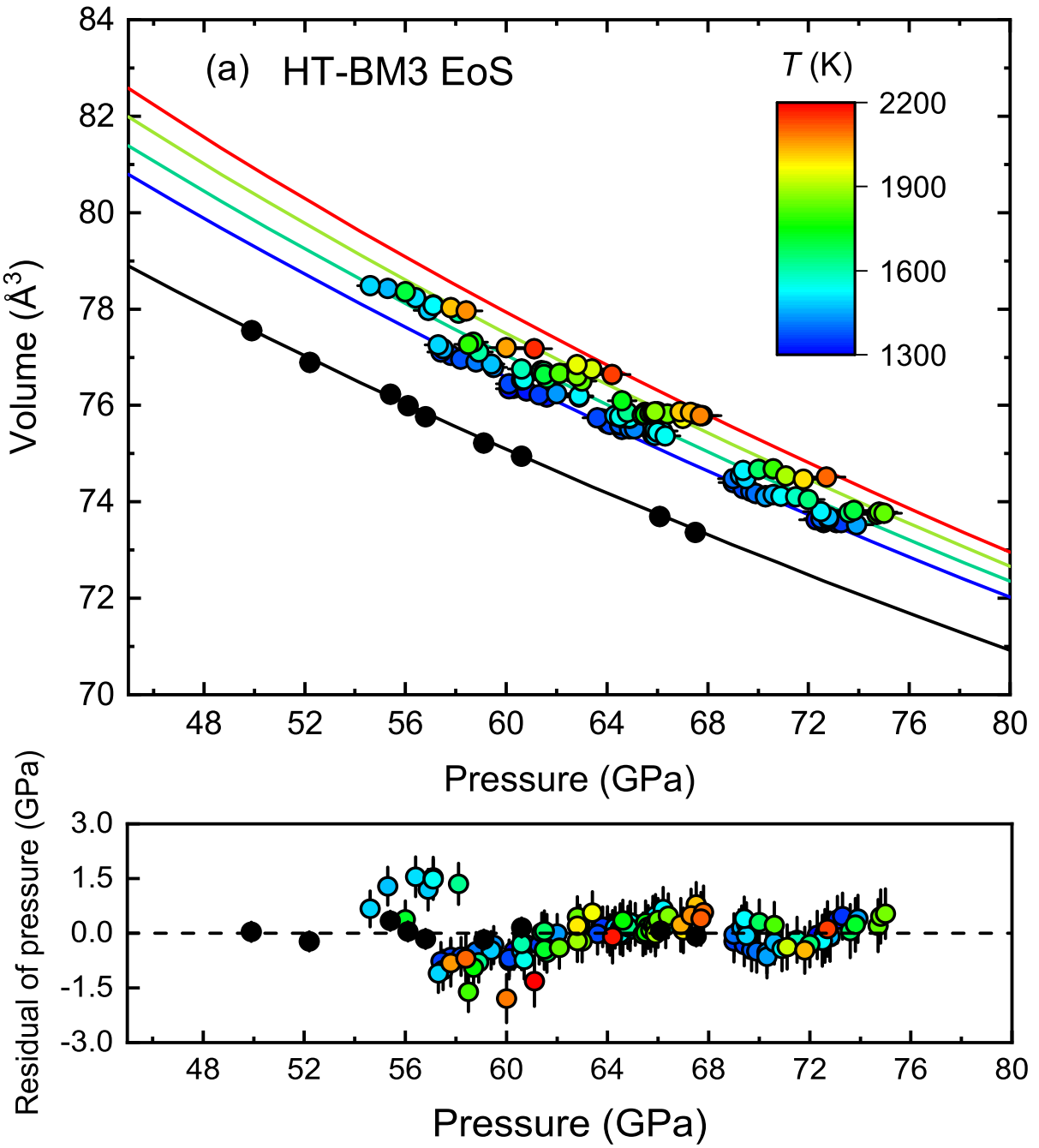
(a) HT-BM3 EoS
T (K)
2200
1900
1600
1300
Volume (Å3)
84
82
80
78
76
74
72
70
48
52
56
60
64
68
72
76
80
Pressure (GPa)
Residual of pressure (GPa)
3.0
1.5
0.0
-1.5
-3.0
48
52
56
60
64
68
72
76
80
Pressure (GPa)

Figure 5(b)

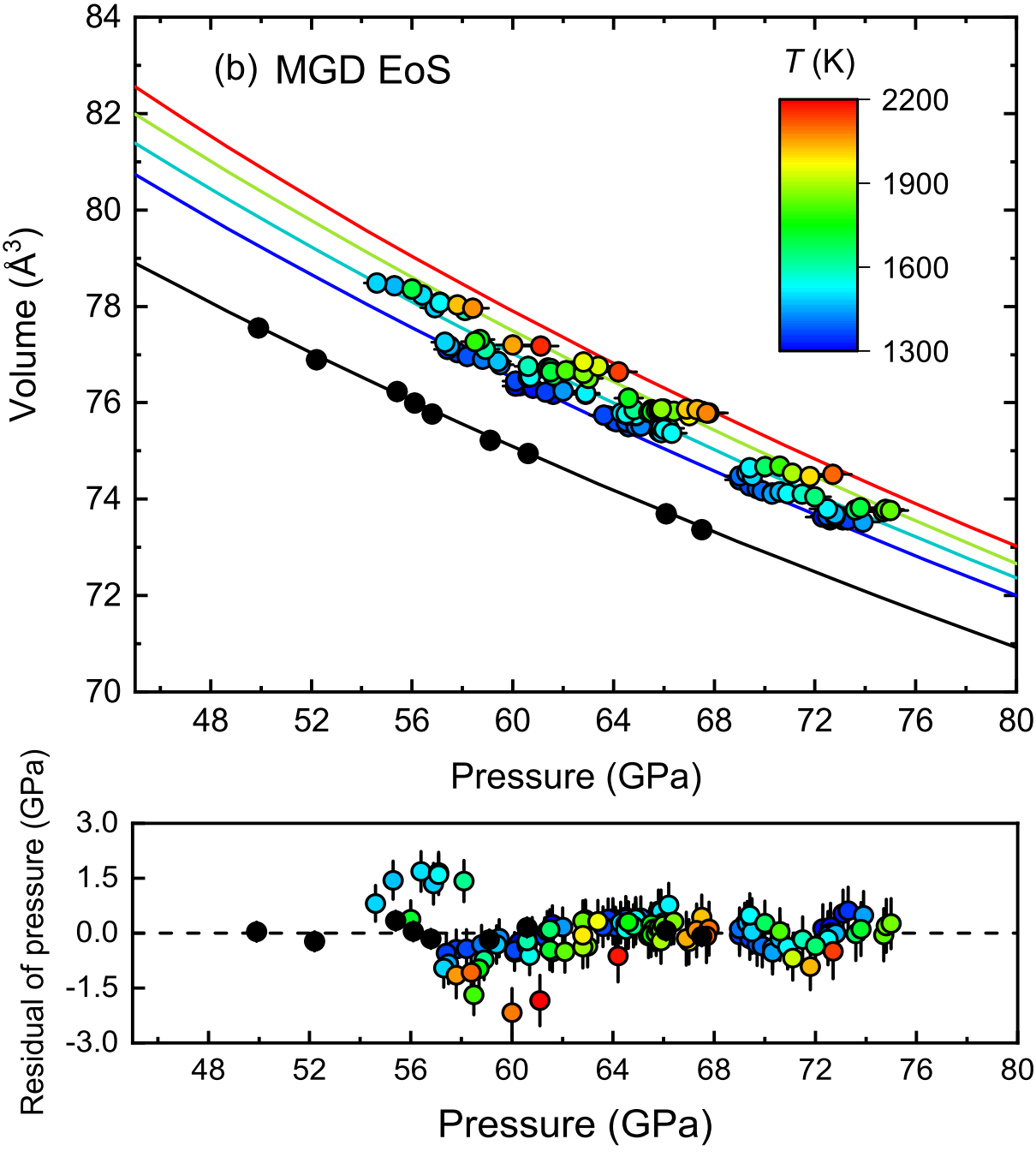
(b) MGD EoS
T (K)
2200
1900
1600
1300
Volume (Å3)
84
82
80
78
76
74
72
70
48
52
56
60
64
68
72
76
80
Pressure (GPa)
Residual of pressure (GPa)
3.0
1.5
0.0
-1.5
-3.0
48
52
56
60
64
68
72
76
80
Pressure (GPa)

Figure 6(a)

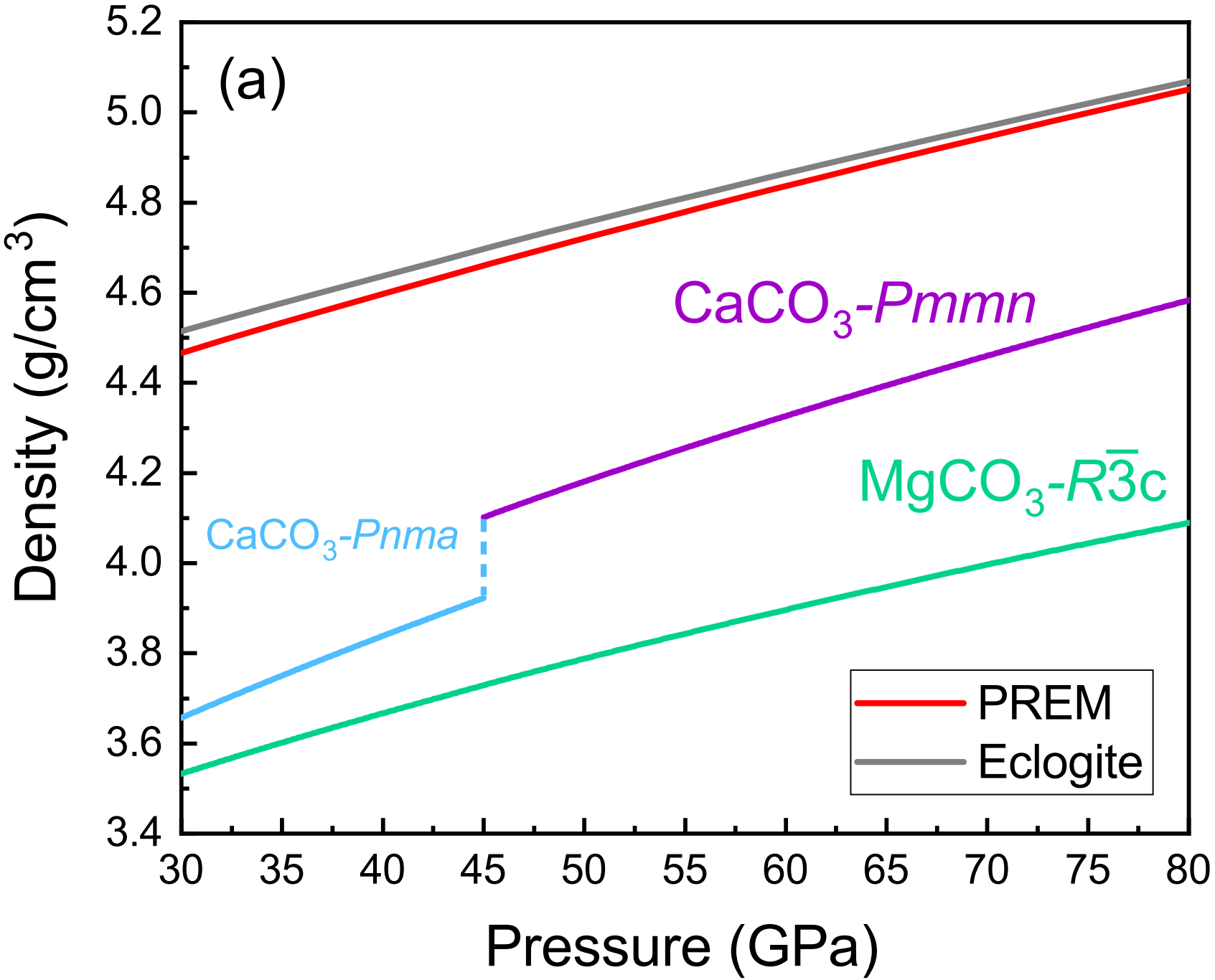
(a)
Density (g/cm^3)
Pressure (GPa)
5.2
5.0
4.8
4.6
4.4
4.2
4.0
3.8
3.6
3.4
30
35
40
45
50
55
60
65
70
75
80
$CaCO_3$-*Pmmn*
$MgCO_3$-$R\bar{3}c$
$CaCO_3$-*Pnma*
PREM
Eclogite

Figure 6(b)

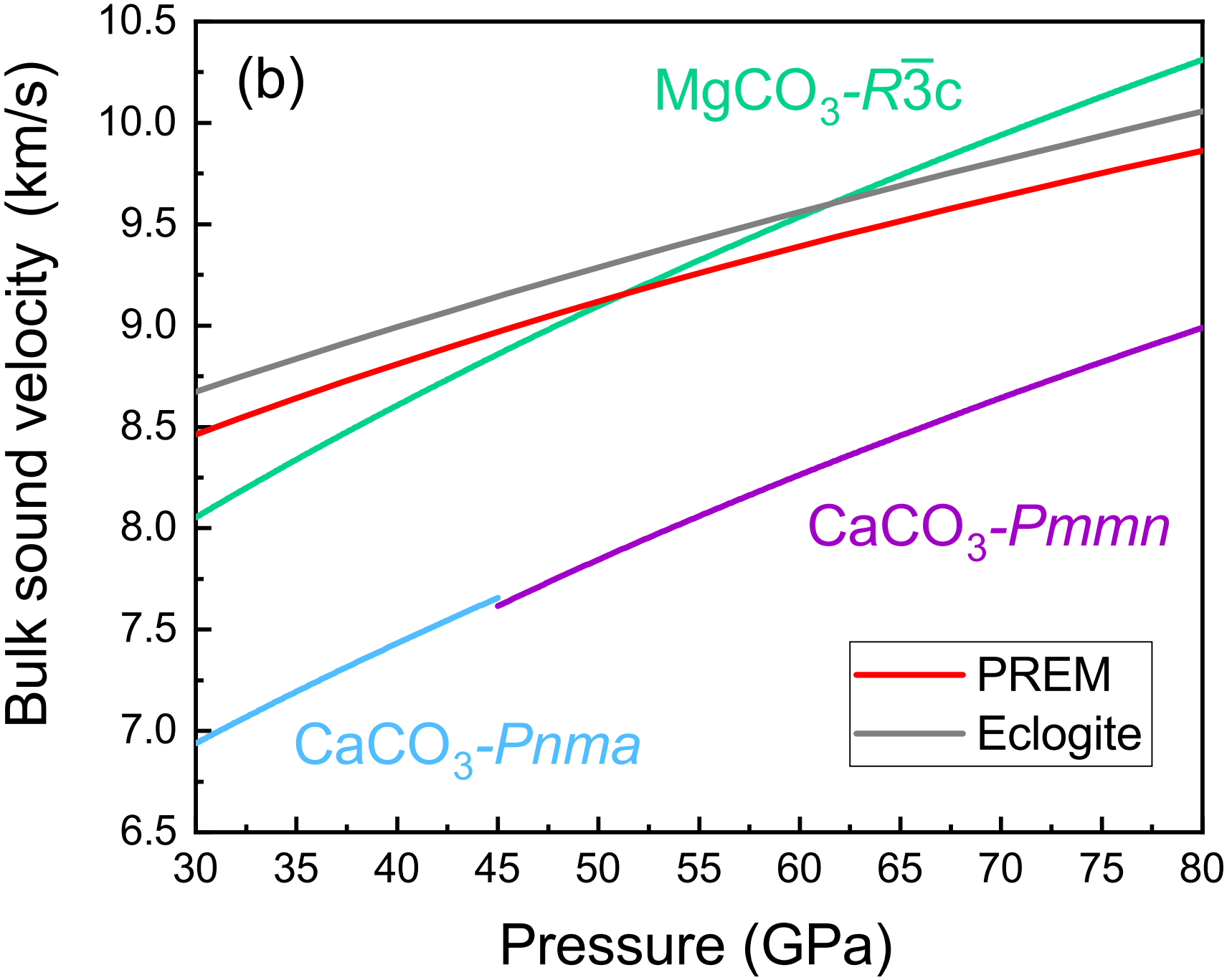
(b)
MgCO3-R3̄c
CaCO3-Pmmn
CaCO3-Pnma
PREM
Eclogite
Bulk sound velocity (km/s)
Pressure (GPa)
10.5
10.0
9.5
9.0
8.5
8.0
7.5
7.0
6.5
30
35
40
45
50
55
60
65
70
75
80

Figure 7(a)

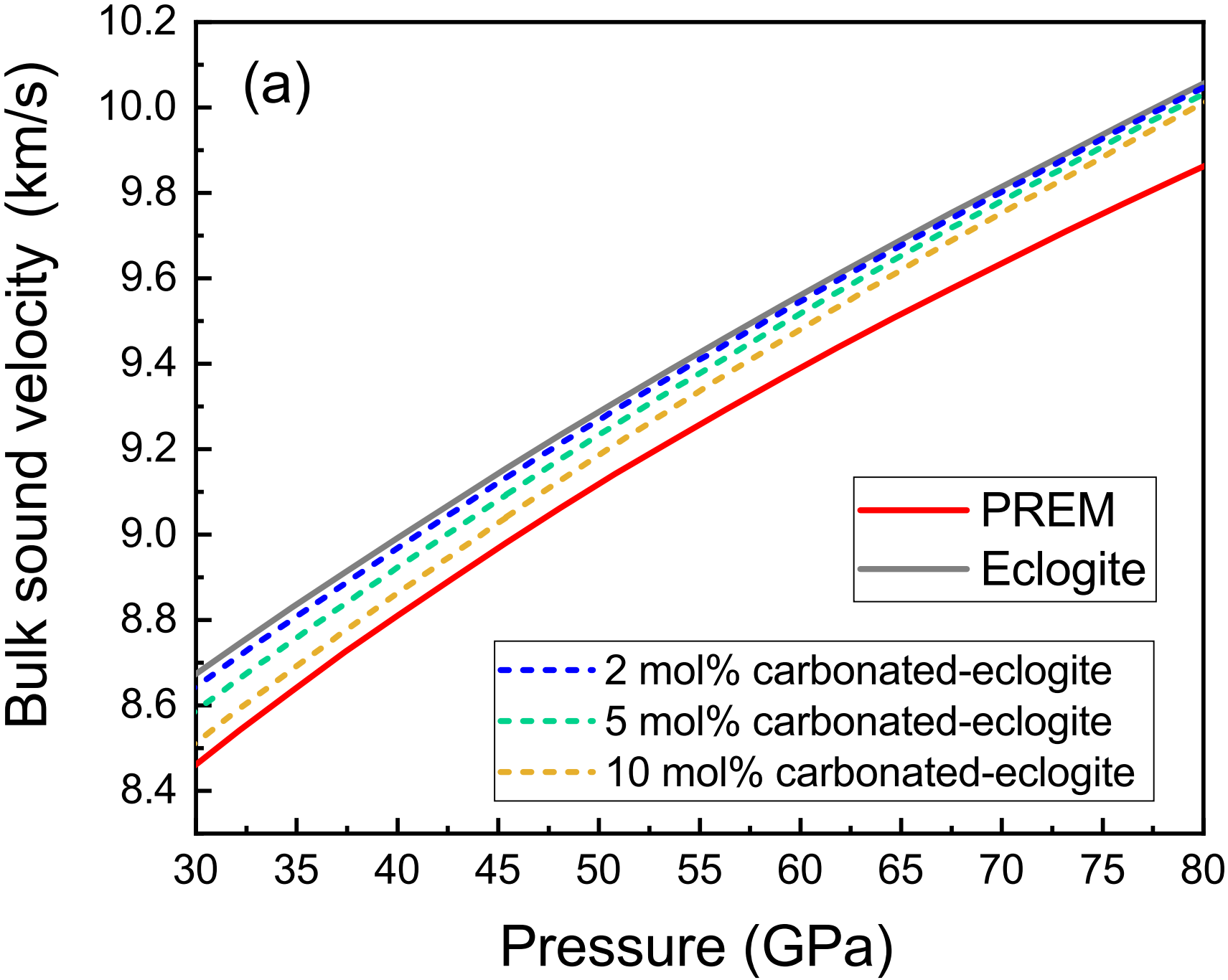
(a)
Bulk sound velocity (km/s)
10.2
10.0
9.8
9.6
9.4
9.2
9.0
8.8
8.6
8.4
30
35
40
45
50
55
60
65
70
75
80
Pressure (GPa)
PREM
Eclogite
2 mol% carbonated-eclogite
5 mol% carbonated-eclogite
10 mol% carbonated-eclogite

Figure 7(b)

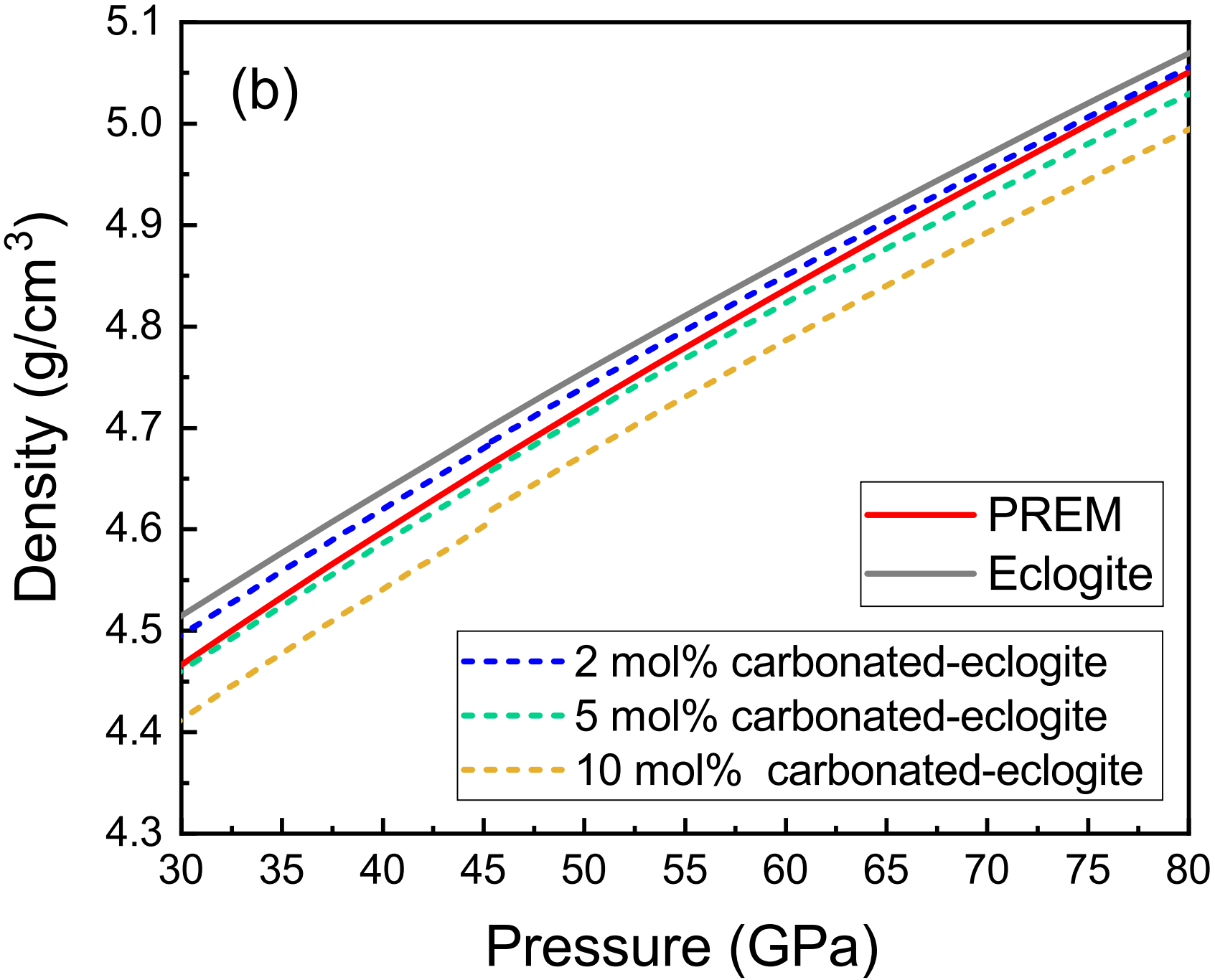
(b)
Density (g/cm^3)
5.1
5.0
4.9
4.8
4.7
4.6
4.5
4.4
4.3
30
35
40
45
50
55
60
65
70
75
80
Pressure (GPa)
PREM
Eclogite
2 mol% carbonated-eclogite
5 mol% carbonated-eclogite
10 mol% carbonated-eclogite